Dynamic interplay between enhancer–promoter topology and gene activity

Hongtao Chen[1], Michal Levo[1], Lev Barinov[2], Miki Fujioka[3], James B. Jaynes [ID][3] and Thomas Gregor [ID][1,4,5]*

A long-standing question in gene regulation is how remote enhancers communicate with their target promoters, and specifically how chromatin topology dynamically relates to gene activation. Here, we combine genome editing and multi-color live imaging to simultaneously visualize physical enhancer–promoter interaction and transcription at the single-cell level in *Drosophila* embryos. By examining transcriptional activation of a reporter by the endogenous *even-skipped* enhancers, which are located 150 kb away, we identify three distinct topological conformation states and measure their transition kinetics. We show that sustained proximity of the enhancer to its target is required for activation. Transcription in turn affects the three-dimensional topology as it enhances the temporal stability of the proximal conformation and is associated with further spatial compaction. Furthermore, the facilitated long-range activation results in transcriptional competition at the locus, causing corresponding developmental defects. Our approach offers quantitative insight into the spatial and temporal determinants of long-range gene regulation and their implications for cellular fates.

Enhancers play a key role in the control of gene expression that is essential for development[1–3]. These 50–1,500 base pair (bp) *cis*-regulatory elements stimulate transcription from core promoters in a time- and tissue-specific manner by recruiting context-dependent transcriptional activators and repressors[4–6]. Whole-genome methods have shown that the human genome is riddled with enhancers, with estimates ranging from 200,000 to over a million[7]. Importantly, a significant fraction of enhancers are located at large genomic distances from the promoters they regulate[8–10]. Even for a compact genome such as *Drosophila melanogaster*, at least 30% of enhancer–promoter interactions occur over 20 kb, and in many cases over intervening genes[11–13].

Despite extensive studies over more than three decades, many questions still remain as to how enhancers communicate with their target promoters over large genomic distances[14]. Static measurements, employing, for example, fluorescence in situ hybridization (FISH) and chromosome conformation capture based genomic experiments, provided evidence supporting physical interactions between a distal enhancer and a target promoter[15–19]. Yet we still lack a dynamic characterization that could distinguish transient contact from the formation of stable topological structures and disentangle cause from consequence in the relationship between such topological structures and transcription. To address these fundamental questions, we have developed a live imaging approach to track the spatial positions of an enhancer and its target promoter and to simultaneously monitor transcriptional activity in developing fly embryos. By employing this approach, we characterize, at the single-cell level, a dynamic interplay between enhancer–promoter topology and transcriptional activity.
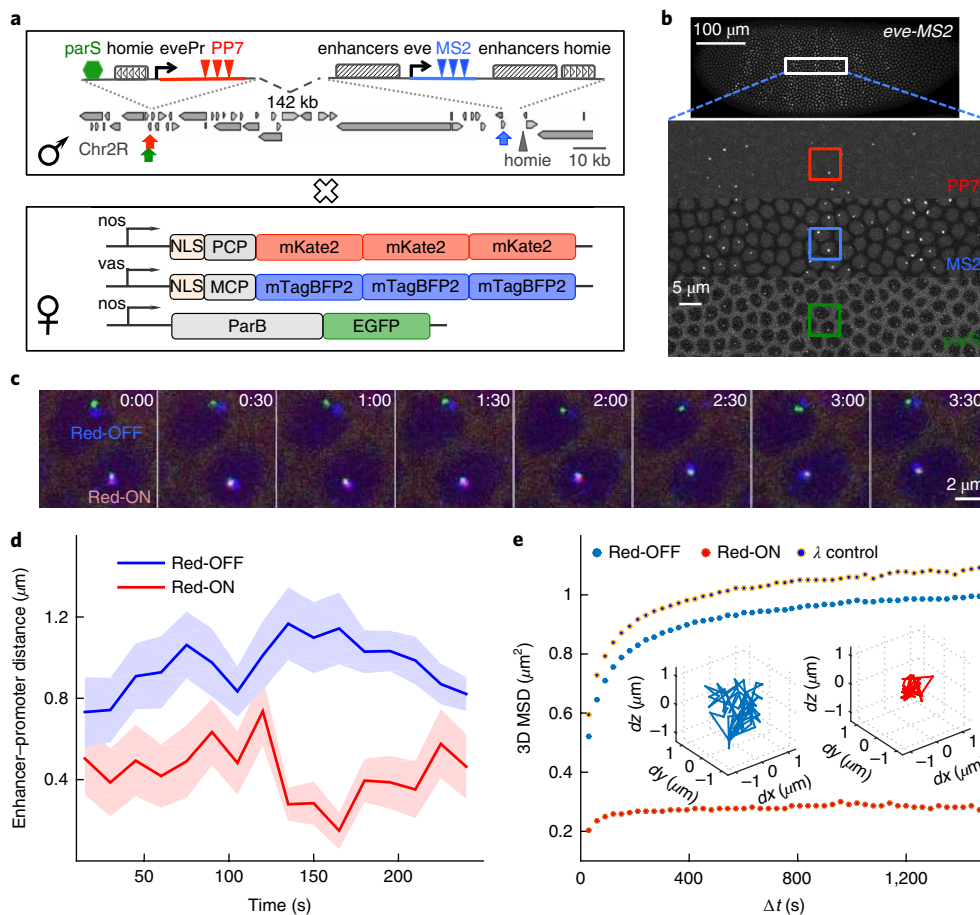
Results

Live imaging of chromatin topology and transcription. To examine long-range transcriptional activation, we placed a reporter gene 142 kb from the well-studied *Drosophila even-skipped (eve)* locus,

which contains a set of five enhancers that drive a seven-striped expression pattern in the cellular blastoderm (Supplementary Fig. 1). While this chosen distance is generally larger than that observed for enhancer–promoter interactions in the early fly embryo, it is comparable to and even smaller than the distances over which many enhancers function in higher eukaryotes[8–10,20]. Notably, at such distance the chromatin fiber can display fast random movements, which creates an entropic hurdle for specific long-range chromatin interactions and thus a kinetic barrier for the establishment of a productive pre-initiation complex. We therefore included in our reporter cassette the 368 bp insulator element *homie* (Supplementary Fig. 1a)[21,22], which facilitates the formation of a stable loop by self-pairing with the endogenous *homie* element[23] located at the 3' end of the *eve* locus[21,22]. In fixed embryos containing our reporter cassette, we observe sporadic expression (~15%) of the reporter gene, solely within the limits of the endogenous *eve* stripes (Supplementary Fig. 1b), which suggests that the reporter is specifically activated by the *eve* enhancers 142 kb away[21].

To simultaneously visualize the location of the endogenous *eve* enhancers, the location of the promoter of the reporter, and its transcriptional activity in living embryos, we designed a three-color imaging system. First, we used two orthogonal stem-loop-based labeling cassettes[24–26]; MS2 stem loops were introduced via CRISPR genome editing to the endogenous *eve* gene, and PP7 stem loops were added to the reporter gene (Fig. 1a, Supplementary Fig. 2a,b, Supplementary Video 1). Maternally expressed fluorescent coat proteins bind the corresponding nascent stem-loops on transcription, providing a dynamic readout of gene activity (Fig. 1a). Owing to the strong transcriptional activity of the *eve* gene, the corresponding fluorescent focus further serves as a marker for the nuclear position of the *eve* enhancers, which are located within 10 kb of the *eve* promoter (Supplementary Fig. 1a). In addition, we took advantage of a recently developed DNA labeling system[27,28] to mark the position of the reporter gene in a manner that is independent of its

Fig. 1 | Three-color live imaging of enhancer–promoter movement and transcriptional activity. a, Male flies carrying the modified *eve* locus are crossed with females carrying maternally expressed blue, red and green fluorescent proteins that are fused to MS2 coat protein (MCP), PP7 coat protein (PCP), and ParB DNA binding protein, respectively. In the male flies, a reporter with an *eve* promoter (*evePr*) driving *PP7* transcription is integrated at −142 kb upstream of an MS2-tagged endogenous *eve* locus in the *Drosophila* genome. An ectopic *homie* insulator sequence is also included in the reporter to force loop formation through *homie-homie* pairing. Furthermore, a *parS* sequence is integrated near the *homie-evePr-PP7* reporter. **b**, Snapshot of a representative embryo generated from crosses shown in **a**. The embryo displays fluorescent foci for MS2, PP7, and parS in the corresponding channels. **c**, Eight snapshots of a time course following two nuclei for ~4 min. The lower nucleus displays *PP7* activity (Red-ON), the upper has none (Red-OFF). **d**, Instantaneous physical enhancer–promoter distance between endogenous *eve* enhancers (blue signal) and the *PP7* reporter (green signal) as a function of time for the Red-OFF and Red-ON nuclei in **c**. Error bar corresponds to measurement error estimated from the co-localization control experiments (see Supplementary Fig. 3). **e**, Population-averaged MSD calculated from enhancer–promoter distance trajectories obtained from all Red-ON ($n = 720$) and Red-OFF ($n = 7{,}163$) nuclei, as well as for a control construct where *homie* in the reporter is replaced by phage λ DNA (λ control, $n = 1{,}453$). Inset shows two representative trajectories for a Red-OFF nucleus (blue) and a Red-ON (red) nucleus, respectively.

activity. Namely, *Burkholderia parS* DNA sequences were included in the reporter gene, nucleating the binding of ParB-GFP fusion proteins (Fig. 1a).

Using three-color time-lapse confocal microscopy, we captured stacks of optical sections of the surface of two-hour-old (nuclear cycle 14, nc14) embryos carrying the tagged *eve* locus and the *parS-homie-evePr-PP7* reporter (Supplementary Video 2). In these stacks, we can clearly identify individual fluorescent foci in 70–100 nuclei simultaneously (Fig. 1b). In the blue channel, we observed the endogenous transcriptional activity of the *eve* gene in its characteristic seven-striped pattern. This pattern is quantitatively identical to that observed from the endogenous *eve* gene (Supplementary Fig. 2c–g, Supplementary Video 1). In the green channel, we observed parB foci in all nuclei of the developing embryo, tracking the position and the movement of the reporter locus (Fig. 1b). Finally, in the red channel, we observed the reporter's transcriptional activity in a subset of nuclei within the (blue) *eve* stripes (Fig. 1b), consistent with our results from fixed embryos (Supplementary Fig. 1b).

These three florescent foci thus provide the means to measure the physical distance between the enhancers and the reporter, as well as to monitor the reporter's transcriptional activity. To ascertain our ability to accurately measure these properties, several control experiments were performed. To estimate the precision of our distance measurements, we generated a synthetic construct (localization control) in which all three fluorescent proteins are co-localized within a genomic distance of 2.0 kb (Supplementary Fig. 3a). By analyzing embryos carrying this construct, we were able to calibrate chromatic aberrations from the microscope and to estimate measurement errors in spot localization (180 ± 6 nm (mean ± s.e.m.), that is, ~75 nm in the *x*/*y* directions and ~150 nm in the axial direction, see Supplementary Fig. 3b–h). Our optical resolution measured from diffraction-limited multi-color fluorescent beads is 20 nm in the *x*/*y* directions and 50 nm in the axial direction (Supplementary Fig. 3b–h). Thus, measurement error originating from optics only accounts for ~10% of the variance in our distance measurement.

We also tested whether our genomic labeling approach introduces perturbations in the system (see experiments and discussion in Supplementary Fig. 4) by (1) removing the maternal ParB supply, (2) placing the parS sequence at different locations relative to the *lacZ* reporter, and (3) employing the more traditional lacO/LacI system instead[29,30]. In no case was the presence of ParB proteins found to affect the activation kinetics of the PP7 reporter (Supplementary Fig. 4e). Furthermore, we did not observe any significant difference in chromatin dynamics or transcription kinetics when the parS tag was placed at different locations or replaced by the lacO tag (Supplementary Fig. 4b–g). These results are consistent with previous studies, in which the parS/ParB system was found to be non-disruptive to chromatin structure[31].

An initial examination of the nuclei in which the PP7 reporter is inactive (Red-OFF) versus those in which it is active (Red-ON) points to a close connection between transcription and the physical proximity of the enhancer–promoter pair (Supplementary Video 3). In Red-OFF nuclei, the reporter is well separated from the *eve* enhancers, while in Red-ON nuclei, all three fluorescent foci appear to be attached together (Fig. 1c). Specifically, when computing the instantaneous spatial distance between the *eve* enhancer and the reporter promoter (that is, the blue to green foci distance, enhancer–promoter distance), a significantly shorter distance is observed for the Red-ON compared to the Red-OFF nuclei (Fig. 1d, Supplementary Fig. 4a–c). Moreover, computing the change in the enhancer–promoter distance across a time interval of variable size gives access to the three-dimensional (3D) mean squared displacement (MSD) for the enhancer–promoter distance trajectories in the two classes of nuclei (Fig. 1e, Supplementary Fig. 4d). The MSD curve reaches a plateau for both types, indicating spatial confinement of the enhancer–promoter distance. Expectedly, the size of this confinement (that is, the spatial limit explored by the enhancer–promoter pair) in the active (Red-ON) nuclei is smaller than that in the inactive (Red-OFF) nuclei (~0.25 versus ~1.0 μm², Fig. 1e).

Necessity of sustained physical proximity for transcription. To assess the temporal relationship between enhancer–promoter proximity and the processes of transcriptional activation and inactivation, we identified all time traces in which we observed nascent transcription in the PP7 reporter gene switching from OFF to ON ($n = 286$) and switching from ON to OFF ($n = 203$), respectively. When we aligned ~20 min time windows of both sets of traces centered around the switching time point, we observed a strong association between physical proximity and activity.

The OFF-to-ON set (Fig. 2a, Supplementary Fig. 5a,b, Supplementary Video 4a–c) displays a sharp transition in transcriptional activity, with rates comparable to those previously reported for active nuclei exiting mitosis[32]. The distance between the *eve* enhancers and the reporter promoter (that is, the blue to green foci distance) converged continuously until this sharp onset of transcription. At this point the enhancer–promoter distance (root-mean-squared (r.m.s.) distance) corresponds to ~340 nm. These findings suggest that enhancer–promoter proximity is required in order to initiate the transgene's transcriptional activity.

Correspondingly, the sharp drop in transcriptional activity observed in the ON-to-OFF set of time traces is accompanied by an increase in the r.m.s. enhancer–promoter distance (Fig. 2b, Supplementary Fig. 5c,d, Supplementary Video 4d–f). While polymerases (RNA polymerase II, PolII) already engaged in transcription will continue to give rise to a detectable red focus even after the separation of the *eve* enhancers from the promoter (probably accounting for the largest part of the observed ~4 min delay[32,33]), it seems transcription initiation ceases as soon as the *eve* enhancers and the reporter promoter physically separate. Overall, these results fit with a model in which sustained enhancer–promoter physical association is necessary for continuous initiation of transcription.

Characterization of three topological states. To establish a quantitative link between physical proximity and transcriptional activity, we constructed the distribution of time-averaged r.m.s. enhancer–promoter distances, across all data acquired. We examined time traces from 7,883 nuclei, across 84 individual embryos, taken over a 30 min period in nc14 and calculated the time-averaged r.m.s. enhancer–promoter distances over a sliding window along each trace (Fig. 3a, Supplementary Fig. 6a, see Methods). We found a bimodal distribution that can be fitted by a mixture of two Gaussians, one harboring 87% of all r.m.s. samples with a mean of 709 ± 110 nm (mean $\pm$ s.d.) and the other, smaller in proportion, with a mean of 353 ± 82 nm.

To gain insight into the topological conformation underlying these two disparate populations, we employed a variant of our reporter construct in which the *homie* sequence is replaced by λ DNA of the same length (*parS-λ-evePr-PP7*). When we constructed the corresponding r.m.s. enhancer–promoter distance distribution from 1,453 nuclei in 15 embryos carrying this construct, we observed a unimodal Gaussian with a mean of 730 ± 112 nm, similar to the large population obtained with the *parS-homie-evePr-PP7* construct (Fig. 3a, Supplementary Fig. 6c). This indicates that the Gaussian with the larger mean, common to both constructs, probably represents nuclei in an open, unpaired conformation. In contrast, the smaller population, with the short enhancer–promoter distances, observed only with the *homie*-containing construct, probably stems from nuclei in a *homie–homie* paired conformation, which are evidently missing in the λ replacement construct. Furthermore, consistent with these postulated underlying conformations, the mean of the large Gaussian increases (that is, shifts to larger distances) when we move the PP7 reporter to a genomic location more distal from the *eve* locus (from −142 to −589 kb, Supplementary Fig. 6d), while the mean of the smaller Gaussian remains unchanged. In addition, the size of the smaller Gaussian is clearly reduced in reporter constructs containing truncated versions of the *homie* element (Supplementary Fig. 7).

Using these distance distributions, we next examined reporter activities. The most noticeable observation stems from the reporter with the λ replacement, in which transcription is largely abolished. This supports the conclusion that sustained proximity is necessary for productive transcription in our system. Indeed, for the *parS-homie-evePr-PP7* construct, the sub-distribution of the enhancer–promoter distances obtained only from time traces displaying PP7 transcriptional activity is fully contained within the smaller Gaussian (red curve in Fig. 3a, Supplementary Fig. 6a), that is, all transcriptionally active reporters are physically close to the *eve* enhancers. However, among all enhancer–promoter distances occupying the small Gaussian, in only 54% is the reporter active (Fig. 3a). The presence of traces in which the promoter is close to the enhancers but nevertheless inactive (green curves, Fig. 3a, Supplementary Fig. 6e) suggests that the proximity obtained by *homie–homie* pairing is not sufficient to ensure transcription. Notably, on *homie–homie* pairing, the linear genomic distance between the reporter promoter and the *eve* enhancers is less than 10 kb, which is similar to the enhancer–promoter distances in the endogenous *eve* locus. Thus, while architectural proteins can bridge the gap between long-range enhancer–promoter interactions (for example, 142 kb) and short-range interactions (for example, 1–10 kb), the facilitated proximity is not sufficient to assure transcription.

Transcription reinforces topological compaction. Our analysis identifies three possible topological states of enhancer–promoter interaction: (1) open conformations that are transcriptionally inactive (O_{off} state), (2) *homie–homie* paired conformations that are transcriptionally inactive (P_{off} state), and (3) *homie-homie* paired conformations that are transcriptionally active (P_{on} state). To assess the physical properties and the transition kinetics of these states, we
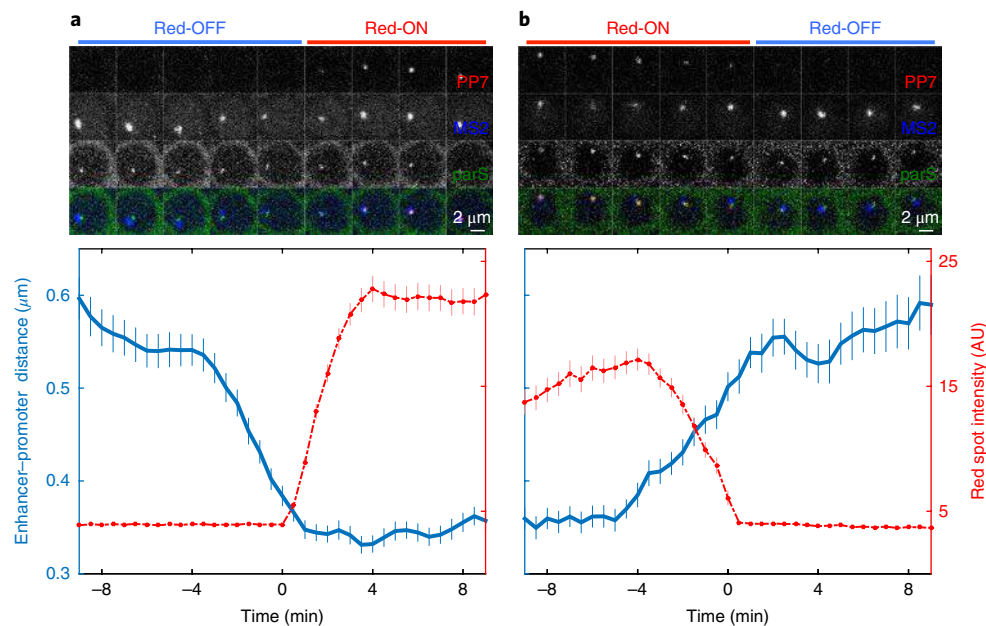
Fig. 2 | Sustained physical enhancer–promoter proximity is necessary for productive transcription. a, Average transcription activity (red) and enhancer–promoter distance (r.m.s. distance between blue and green foci) as a function of time for 286 nuclei transitioning from the Red-OFF to Red-ON state (red spot intensity in arbitrary units (AU)). Time series for individual nuclei are aligned such that *PP7* activity starts at 0 min, that is, first occurrence of red signal. Top panel shows a series of raw images of a representative nucleus that transitions from Red-OFF to Red-ON (see also Supplementary Video 4). **b**, Average transcription activity and enhancer–promoter distance as a function of time for 203 nuclei transitioning from Red-ON to Red-OFF. Time series for individual nuclei are aligned such that *PP7* activity ends at 0 min, that is, disappearance of red signal. The top panel shows a series of raw images of a representative nucleus that transitions from Red-ON to Red-OFF (see also Supplementary Video 4). All error bars are standard errors of the mean.

assigned each time point of the 7,883 time traces to one of the three states. Specifically, we used a Bayes classifier to distinguish between the unpaired and the paired state, using time traces from the *parS-λ-evePr-PP7* construct for the open state (O) and time traces with PP7 activity for the paired state (P) as training samples. Furthermore, we used the presence of the PP7 (red) signal to further divide the paired state (P) into an inactive P_{off} state and an active P_{on} state (Supplementary Fig. 8a–j; for details see Methods).

When we compared the distance distribution of the inactive paired (P_{off}) and the active paired (P_{on}) states, we found that the mean ($\pm$s.d.) r.m.s. enhancer–promoter distance for the P_{off} state (385 ± 15 nm) is significantly larger than for the P_{on} state (331 ± 16 nm) (Fig. 3d, Supplementary Fig. 8k). The shorter r.m.s. distance in the transcriptionally active state is indicative of an enhanced compaction of the locus when the reporter is active.

To further examine the relationship between compaction and transcription, we employed an additional variant of our reporter cassette, in which we deleted the promoter from our transgene (*parS-homie-noPr-PP7*). The r.m.s. enhancer–promoter distance distribution for this construct recovers the bi-modal distribution from the original construct representing the O_{off} and P_{off} states (calculated from 2,566 nuclei in 29 embryos, Fig. 3a, Supplementary Fig. 6b). In particular, the mean r.m.s. enhancer–promoter distance of the P_{off} state measured for this promoter-less construct (374 ± 14 nm, mean $\pm$ s.d.) coincides with that measured for the full construct (Fig. 3c, Supplementary Fig. 8k), and is thus larger than that of the P_{on} population (Fig. 3d, Supplementary Fig. 8k). Together, these results argue for the association of transcription with a smaller physical confinement.

Transcription enhances stability of the paired conformation.
Interestingly, we found that the *parS-homie-noPr-PP7* construct, which is non-permissive for transcription, has a smaller fraction

of the population in the *homie* paired conformation (P state) than does the *parS-homie-evePr-PP7* construct, which is permissive for transcription (8% versus 13%, Fig. 3c,d). This suggests that transcription is not only associated with a more confined spatial conformation but may also be associated with a temporal stabilization of the paired conformation.

In order to test this, we use a set of first-order reactions to model the kinetic transitions between the three topological states described above (Fig. 3e, Supplementary Fig. 9a, see Methods). Using this model, we determined the transition rates by fitting the model-derived equations to the measured time courses of the fractional occupancies for each of the three states (Fig. 3e, Supplementary Fig. 9a–h). The transition from an open topology to the *homie-homie* pairing state ($f_1 = 0.017$ min^{-1}, see Fig. 3e inset) takes on average 1 h. This rate is ~8 times slower than the time it takes for the enhancer to explore the entire confined space in the vicinity of the promoter in the *parS-λ-evePr-PP7* construct, as predicted by our MSD results, assuming a simple first-passage model[34] (where the time $t = (MSD/6D)^{1/\alpha}$, in which MSD is the λ control plateau in Fig. 1e, D is the apparent diffusion coefficient and α is the scaling constant, see Supplementary Fig. 4d). It is possible that the *homie* orientation preference for pairing[23] (as was also described for other architectural factors, such as CTCF[35,36]) constrains productive passages, thereby contributing to this slower rate. Notably, this rate of pairing is roughly an order of magnitude slower than the rapid transcriptional events that take place in the early fly embryo. This requirement of rapidity is possibly facilitated by closer enhancer–promoter distances, characteristic of early developmental genes, than the 142 kb that we explored here.

Examining the other transition rates obtained from our model (see Fig. 3e inset) confirms the stabilizing effect of transcription on locus topology: the dissociation of the *homie–homie* pairing complex in the absence of transcription ($b_1 = 0.144$ min^{-1}) is on average
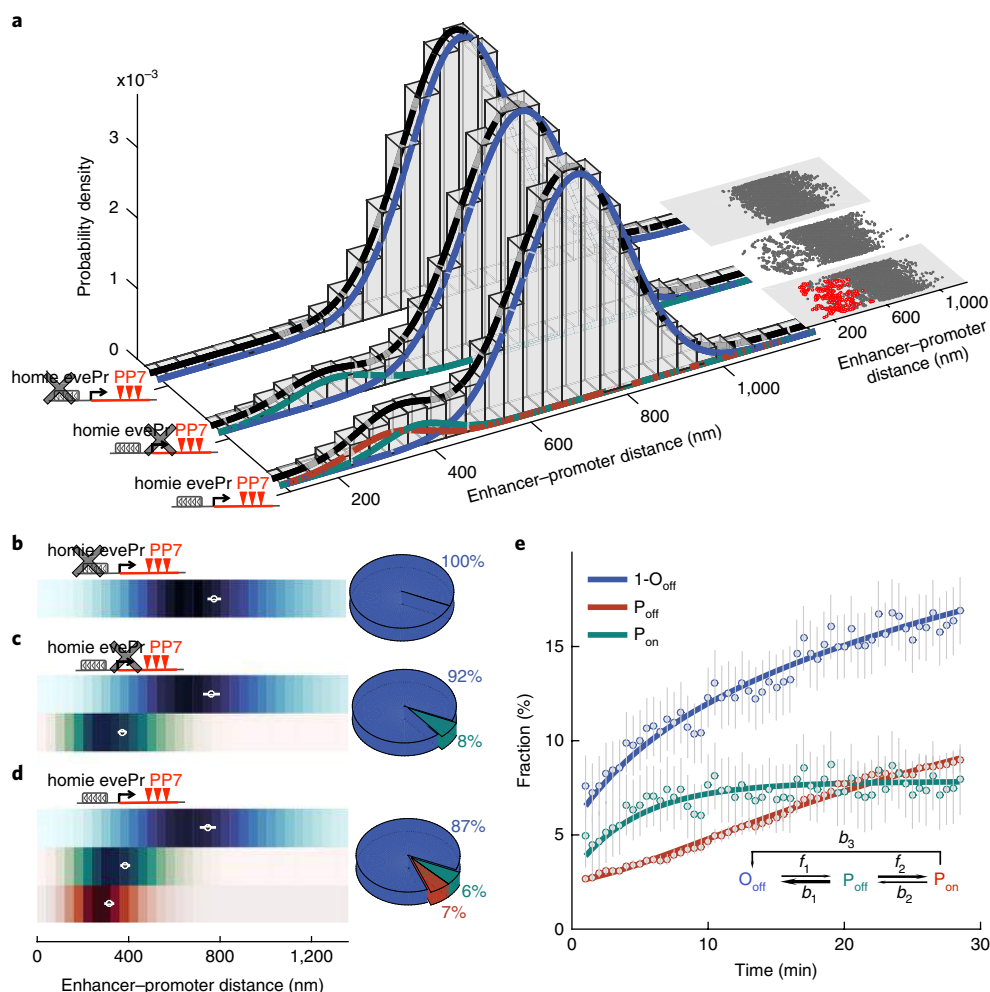
Fig. 3 | Characterization of topological enhancer–promoter conformations, the kinetic transitions between them, and their relation to transcriptional activation. a, Enhancer–promoter distance distribution for three experimental constructs: *parS-homie-evePr-PP7* ($n = 265,277$ r.m.s. enhancer–promoter distances from 7,883 trajectories in 84 embryos), *parS-homie-noPr-PP7* ($n = 81,629$ r.m.s. enhancer–promoter distances from 2,566 trajectories in 29 embryos) and *parS-λ-evePr-PP7* ($n = 49,587$ r.m.s. enhancer–promoter distances from 1,453 trajectories in 15 embryos); black cross on construct label indicates deleted element from original. A 5-min sliding window along each time trace is used to calculate r.m.s. enhancer–promoter distances. Gaussian mixture models for all r.m.s. samples are shown with black curves for each construct. Gaussian mixture models for r.m.s. samples in which PP7 is not active are shown with blue (larger mean) and green (smaller mean) curves. Red curve is Gaussian fitting for all r.m.s. distance samples accompanied by continuous PP7 transcription. Insets show scatter plots of r.m.s. distance from one representative embryo for each construct. Each data point is a time-averaged r.m.s. distance. Red points indicate continuous PP7 transcription across the window. **b–d**, Distribution of instantaneous enhancer–promoter distance for enhancer–promoter topological states classified as O_{off} (blue), P_{off} (green) or P_{on} (red) for *parS-λ-evePr-PP7* (**b**), *parS-homie-noPr-PP7* (**c**) and *parS-homie-evePr-PP7* (**d**). Means ± s.d. of r.m.s. distance calculated from individual embryos shown as white circles with bars. Adjacent pie charts show the fraction of each enhancer–promoter topological state. See also Supplementary Figure 8. **e**, Fraction of each topological state for the *parS-homie-evePr-PP7* construct as a function of developmental time, starting 25 min into nc14. Error bars are bootstrapped standard errors of state fractions. Solid lines are fits derived from kinetic parameters obtained from MCMC (Markov Chain Monte Carlo) inference. Inset shows the kinetic model capturing the transitions between the three topological states; arrow widths represent transition time scales (wider arrows correspond to faster rates, see Supplementary Fig. 9 for values).

over ten times faster than the escape from the transcriptionally active state P_{on} ($b_2 = 0.014$ min^{-1}, $b_3 = 0.011$ min^{-1}, Supplementary Fig. 9e–g). These rates capture the escape from the transcriptionally active state P_{on} (b_2 and b_3) and recapitulate quantitatively the measured durations of transcriptional activity (length of Red-ON trajectories, Supplementary Fig. 9h). Intriguingly, the average duration of the transcriptionally active state is about 40 min ($1/(b_2 + b_3)$), which coincides with the length of the developmental time window in which the *eve* stripe enhancers are active in nc14. This transcription-dependent stabilization might thus serve to reinforce the locus functionality for the appropriate developmental time scales.

Ectopic enhancer–promoter interaction results in developmental defects. In our experiments, the *eve* stripe enhancers, distributed within the ~16 kb of the *eve* locus (Supplementary Fig. 1a), drive expression of both the introduced reporter gene and the endogenous *eve* gene, which could possibly lead to competitive dynamics. To test this hypothesis, we compared *eve* transcriptional activity (that is, the intensity of the blue MS2 signal) in each individual nucleus in which the PP7 reporter gene is active to the activity in its neighboring nuclei in which the reporter is inactive (Fig. 4a, see Methods). Strikingly, for each *eve* stripe, we measured a 5%–20% reduction in endogenous *eve* transcription in nuclei in which the reporter gene is
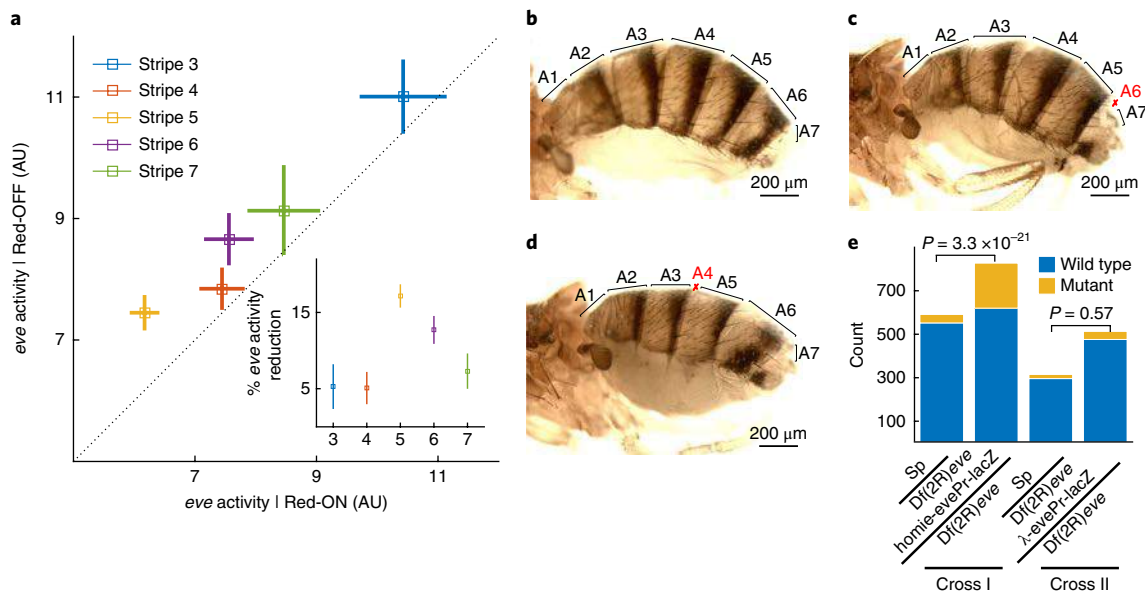
Fig. 4 | Long-distance-mediated promoter competition results in patterning phenotypes. a, Endogenous *eve-MS2* activity in nuclei that also display *PP7* reporter activity (*x* axis) is lower than in the neighboring nuclei where *PP7* is not expressed (*y* axis). Means ± s.e.m. (*n* = 45, 106, 143, 85 and 27 *PP7* expressing nuclei for stripe 3–7, respectively). Inset: Reduction in *eve-MS2* activity for each stripe. Error bars are bootstrapped standard errors of the percentage reduction. **b–d**, Adult wild-type (**b**) and mutant (**c**, **d**) flies from crosses between *Sp/homie-evePr-lacZ* males and *CyO/Df*(2R)*eve⁻* females. **c** and **d** show defects in abdominal segments A4 and A6, respectively, resulting from reduced *eve* activity in stripe 5 and stripe 6, respectively. Abdominal segments are labeled, with defective segments marked in red. **e**, Results of phenotype scoring. Mutant counts include both A4 and A6 phenotypes. Cross I: single *Sp/homie-evePr-lacZ* males were crossed with *CyO/Df*(2R)*eve⁻* females, and scoring results from 47 individual vials were summed. Cross II: single *Sp/λ-evePr-lacZ* males were crossed with *CyO/Df*(2R)*eve⁻* females, and results from 23 individual vials were summed. *P* values are from one-tailed Fisher's exact test.

also transcribed compared to neighboring nuclei in which it is not transcribed. The average reduction per nucleus is highest for stripe 5, and lowest for stripes 3 and 7.

eve is a primary pair-rule gene that is essential for segment patterning, allowing us to test whether the observed reduction in *eve* transcription has a phenotypic consequence. We crossed males carrying a tag-less *homie-evePr-lacZ* transgene at −142 kb to females heterozygous for a wild-type *eve* gene and an *eve* deficiency (Df(2R)*eve*) (Supplementary Fig. 10a). *eve* is weakly haploinsufficient and 6% of +/*Df*(2R)*eve* flies display patterning defects in even-numbered parasegments (Supplementary Fig. 10b–e). Consistent with the reduction in the level of *eve* nascent transcripts, the presence of the *homie-evePr-lacZ* transgene exacerbates *eve* haploinsufficiency (Fig. 4b–d, Supplementary Fig. 10a). Altogether, 27% of the *homie-evePr-lacZ/Df*(2R)*eve* flies have abdominal defects, which corresponds to a ~5-fold increase compared with the control crosses in which *homie* is replaced by phage λ DNA (Fig. 4e, Supplementary Fig. 10a). Taken together, these results suggest that interference between two promoters in the early embryo can have phenotypic consequences for patterning in the adult. These findings reinforce the view that manipulating topological chromatin structures can functionally alter developmental programs[37,38].

Discussion

Simultaneous multi-color live imaging of gene activity and the positions of genomic foci identifies a dynamic interplay between chromatin topology and transcriptional activity. By analyzing this interplay, we identify a requirement for a distinct topological structure that brings promoter and distant enhancer together in the nucleus, formed through pairing of insulator elements, for the initiation and maintenance of transcription. The temporal concordance between cessation of transcription and physical dissociation of this paired conformation argues against a suggested 'hit-and-run'

model and argues in favor of the requirement for persistent physical enhancer–promoter proximity for sustained transcription.

Notably, the physical proximity attained by insulator pairing is not a guarantee for transcriptional activation. This observation will prompt further investigation as to the mechanisms underlying the transition to an active state. These might involve a second, entropy-based search step resulting in direct physical contact between the enhancer and promoter, and/or entail transcription factor binding with the involvement of other components of the transcription machinery (for example, mediator, PolII pause-release), or a change in local chromatin accessibility, each of which was previously associated with transitions from a transcriptionally 'off' to an 'on' state[12,39–43].

Our measurements provide further insights into the open debate on whether topological changes precede transcription[44,45]. Specifically, our results argue for a complex interplay, as we observe a transcription-mediated reshaping of the kinetic landscape of 3D genome organization. While transcription seems to require physical proximity, it is in turn associated with further spatial compaction and temporal stabilization. It is possible that transcription can only occur within close proximity (even within the range of P_{off} distances), and that the observed spatial compaction could result from a biased sampling of the P_{off} distribution by transcription and not necessarily an active mechanism of compaction. The observed compaction is also consistent with recently proposed hypotheses that phase behaviors might contribute to the formation of Pol II 'factories' or transcription 'hubs' within topologically associated domains[46–48].

Overall, we identify and characterize three states; one in which the distal enhancer and the promoter are not together (O_{off}), a second in which they are 'within range' (as afforded by insulator pairing) but the gene is transcriptionally inactive (P_{off}), and a third, which seems stabilized by transcriptional activation (P_{on}), and in

which they are close together. These results are consistent with several recent observations obtained from fixed samples, including observations of proximity of an enhancer to a promoter prior to activation[12] and of an increase in co-localization in expressing tissues[49]. Our observations suggesting that transcription is associated with a different 3D landscape are also in line with recent Hi-C experiments carried out in the early *Drosophila* embryo, in which the authors suggest an effect of transcription on local chromatin organization, such as co-localization of boundaries and local compaction[44].

Interestingly, topological domain boundaries, as captured by recent early embryo Hi-C experiments, coincide with DNA regions that are rich in insulator protein binding[44,50]. Indeed, previous studies showed that insulator proteins demarcate regulatory units of the fly genome, often separating differentially expressed genes[51]. These proteins have been suggested not only to contribute to the formation of boundaries but also to facilitate physical interactions between boundaries to form "loop domains"[44,50], probably through protein pairing[52]. Importantly, such interactions between insulators were specifically also implicated in mediating long-range activation[52,53]. While such long-range interactions might not be ubiquitous in the very early embryo undergoing rapid nuclear divisions (0–2 h), in slightly older embryos (3–8 h) they were found to be prevalent (with a reporter median distance of 110 kb)[12].

Our observation of a nearly inactive reporter at a distance of ~140 kb in the absence of the *homie* insulator suggests the necessity of these architectural elements in mediating long-range activation. Naturally, the exact properties of such elements could differ, affecting, for instance, the likelihood of pairing even on an encounter (for example, depending on orientation preferences) and the stability of the paired configuration. Such differences could then influence to some degree the kinetics of transcription (for example, affecting the rate of escape from the paired transcribing state). In the constructs presented here, we chose to include the *homie* element, due a documented role in the endogenous *eve* locus[22]. This allowed us to obtain pairing over long distances and thereby enabled our live examination of enhancer–promoter interactions, linking 3D topology and transcription. The overall landscape of the fly genome, as it emerges from mapping insulator binding, chromosome conformation capture experiments, and locus-specific studies, suggests that our genomic constructs (with activation over >100-kb distance, and with physical proximity facilitated by insulator pairing) are capturing fundamental properties of long-range activation in flies, and probably also in other higher eukaryotes.

Finally, we show that a perturbation involving long-range activation by an endogenous enhancer can have clear phenotypic implications. This strengthens previous observations linking disease and aberrant transcription to 3D genome structure[38,54], and highlights the necessity of methods to mechanistically study these links[55]. Extensions of our approach to study different genes, regulated by enhancers at different distances, whose interaction is mediated by different architectural proteins, and in various developmental stages and organisms, will thus probably uncover new mechanistic insights into enhancer–promoter interactions.

Methods

References

1. Benoist, C. & Chambon, P. In vivo sequence requirements of the SV40 early promotor region. *Nature* **290**, 304–310 (1981).
2. Levine, M. Transcriptional enhancers in animal development and evolution. *Curr. Biol.* **20**, R754–R763 (2010).
3. Long, H. K., Prescott, S. L. & Wysocka, J. Ever-changing landscapes: transcriptional enhancers in development and evolution. *Cell* **167**, 1170–1187 (2016).
4. Buecker, C. & Wysocka, J. Enhancers as information integration hubs in development: lessons from genomics. *Trends Genet.* **28**, 276–284 (2012).
5. Kim, T. K. & Shiekhattar, R. Architectural and functional commonalities between enhancers and promoters. *Cell* **162**, 948–959 (2015).
6. Vernimmen, D. & Bickmore, W. A. The hierarchy of transcriptional activation: from enhancer to promoter. *Trends Genet.* **31**, 696–708 (2015).
7. Consortium, E. P. An integrated encyclopedia of DNA elements in the human genome. *Nature* **489**, 57–74 (2012).
8. Tolhuis, B., Palstra, R. J., Splinter, E., Grosveld, F. & de Laat, W. Looping and interaction between hypersensitive sites in the active beta-globin locus. *Mol. Cell.* **10**, 1453–1465 (2002).
9. Uslu, V. V. et al. Long-range enhancers regulating Myc expression are required for normal facial morphogenesis. *Nat. Genet.* **46**, 753–758 (2014).
10. Zhang, Y. et al. Chromatin connectivity maps reveal dynamic promoter-enhancer long-range associations. *Nature* **504**, 306–310 (2013).
11. Arnold, C. D. et al. Genome-wide quantitative enhancer activity maps identified by STARR-seq. *Science* **339**, 1074–1077 (2013).
12. Ghavi-Helm, Y. et al. Enhancer loops appear stable during development and are associated with paused polymerase. *Nature* **512**, 96–100 (2014).
13. Kvon, E. Z. et al. Genome-scale functional characterization of *Drosophila* developmental enhancers in vivo. *Nature* **512**, 91–95 (2014).
14. Levine, M., Cattoglio, C. & Tjian, R. Looping back to leap forward: transcription enters a new era. *Cell* **157**, 13–25 (2014).
15. Kagey, M. H. et al. Mediator and cohesin connect gene expression and chromatin architecture. *Nature* **467**, 430–435 (2010).
16. Mifsud, B. et al. Mapping long-range promoter contacts in human cells with high-resolution capture Hi-C. *Nat. Genet.* **47**, 598–606 (2015).
17. Andrey, G. et al. A switch between topological domains underlies HoxD genes collinearity in mouse limbs. *Science* **340**, 1234167 (2013).
18. Spitz, F. Gene regulation at a distance: from remote enhancers to 3D regulatory ensembles. *Semin. Cell Dev. Biol.* **57**, 57–67 (2016).
19. Carter, D., Chakalova, L., Osborne, C. S., Dai, Y. F. & Fraser, P. Long-range chromatin regulatory interactions in vivo. *Nat. Genet.* **32**, 623–626 (2002).
20. Sanyal, A., Lajoie, B. R., Jain, G. & Dekker, J. The long-range interaction landscape of gene promoters. *Nature* **489**, 109–113 (2012).
21. Fujioka, M., Wu, X. & Jaynes, J. B. A chromatin insulator mediates transgene homing and very long-range enhancer-promoter communication. *Development* **136**, 3077–3087 (2009).
22. Fujioka, M., Sun, G. & Jaynes, J. B. The *Drosophila* eve insulator Homie promotes *eve* expression and protects the adjacent gene from repression by polycomb spreading. *PLoS Genet.* **9**, e1003883 (2013).
23. Fujioka, M., Mistry, H., Schedl, P. & Jaynes, J. B. determinants of chromosome architecture: insulator pairing in *cis* and in *trans*. *PLoS Genet.* **12**, e1005889 (2016).
24. Larson, D. R., Zenklusen, D., Wu, B., Chao, J. A. & Singer, R. H. Real-time observation of transcription initiation and elongation on an endogenous yeast gene. *Science* **332**, 475–478 (2011).
25. Hocine, S., Raymond, P., Zenklusen, D., Chao, J. A. & Singer, R. H. Single-molecule analysis of gene expression using two-color RNA labeling in live yeast. *Nat. Methods* **10**, 119–121 (2013).
26. Fukaya, T., Lim, B. & Levine, M. Enhancer control of transcriptional bursting. *Cell* **166**, 358–368 (2016).
27. Dubarry, N., Pasta, F. & Lane, D. ParABS systems of the four replicons of Burkholderia cenocepacia: new chromosome centromeres confer partition specificity. *J. Bacteriol.* **188**, 1489–1496 (2006).
28. Saad, H. et al. DNA dynamics during early double-strand break processing revealed by non-intrusive imaging of living cells. *PLoS Genet.* **10**, e1004187 (2014).
29. Gasser, S. M. Visualizing chromatin dynamics in interphase nuclei. *Science* **296**, 1412–1416 (2002).
30. Sinclair, P., Bian, Q., Plutz, M., Heard, E. & Belmont, A. S. Dynamic plasticity of large-scale chromatin structure revealed by self-assembly of engineered chromosome regions. *J. Cell Biol.* **190**, 761–776 (2010).
31. Bystricky, K. Chromosome dynamics and folding in eukaryotes: insights from live cell microscopy. *FEBS Lett.* **589**, 3014–3022 (2015).
32. Garcia, H. G., Tikhonov, M., Lin, A. & Gregor, T. Quantitative imaging of transcription in living *Drosophila* embryos links polymerase activity to patterning. *Curr. Biol.* **23**, 2140–2145 (2013).
33. Fukaya, T., Lim, B. & Levine, M. Rapid rates of Pol II elongation in the *Drosophila* embryo. *Curr. Biol.* **27**, 1387–1391 (2017).
34. Lucas, J. S., Zhang, Y., Dudko, O. K. & Murre, C. 3D trajectories adopted by coding and regulatory DNA elements: first-passage times for genomic interactions. *Cell* **158**, 339–352 (2014).

35. Guo, Y. et al. CRISPR inversion of CTCF sites alters genome topology and enhancer/promoter function. *Cell* **162**, 900–910 (2015).
36. Rao, S. S. et al. A 3D map of the human genome at kilobase resolution reveals principles of chromatin looping. *Cell* **159**, 1665–1680 (2014).
37. Deng, W. et al. Reactivation of developmentally silenced globin genes by forced chromatin looping. *Cell* **158**, 849–860 (2014).
38. Franke, M. et al. Formation of new chromatin domains determines pathogenicity of genomic duplications. *Nature* **538**, 265–269 (2016).
39. Dixon, J. R. et al. Chromatin architecture reorganization during stem cell differentiation. *Nature* **518**, 331–336 (2015).
40. Krijger, P. H. et al. Cell-of-origin-specific 3D genome structure acquired during somatic cell reprogramming. *Cell Stem Cell* **18**, 597–610 (2016).
41. Raser, J. M. & O'Shea, E. K. Control of stochasticity in eukaryotic gene expression. *Science* **304**, 1811–1814 (2004).
42. Voss, T. C. & Hager, G. L. Dynamic regulation of transcriptional states by chromatin and transcription factors. *Nat. Rev. Genet.* **15**, 69–81 (2014).
43. Sanchez, A., Garcia, H. G., Jones, D., Phillips, R. & Kondev, J. Effect of promoter architecture on the cell-to-cell variability in gene expression. *PLoS Comput. Biol.* **7**, e1001100 (2011).
44. Hug, C. B., Grimaldi, A. G., Kruse, K. & Vaquerizas, J. M. Chromatin architecture emerges during zygotic genome activation independent of transcription. *Cell* **169**, 216–228 e19 (2017).
45. Rubin, A. J. et al. Lineage-specific dynamic and pre-established enhancer-promoter contacts cooperate in terminal differentiation. *Nat. Genet.* **49**, 1522–1528 (2017).
46. Hnisz, D., Shrinivas, K., Young, R. A., Chakraborty, A. K. & Sharp, P. A. A phase separation model for transcriptional control. *Cell* **169**, 13–23 (2017).
47. Sexton, T., Umlauf, D., Kurukuti, S. & Fraser, P. The role of transcription factories in large-scale structure and dynamics of interphase chromatin. *Semin. Cell Dev. Biol.* **18**, 691–697 (2007).
48. Cho, W. K. et al. RNA polymerase II cluster dynamics predict mRNA output in living cells. *eLife* **5**, e13617 (2016).
49. Williamson, I., Lettice, L. A., Hill, R. E. & Bickmore, W. A. Shh and ZRS enhancer colocalisation is specific to the zone of polarising activity. *Development* **143**, 2994–3001 (2016).
50. Stadler, M. R., Haines, J. E. & Eisen, M. B. Convergence of topological domain boundaries, insulators, and polytene interbands revealed by high-resolution mapping of chromatin contacts in the early *Drosophila melanogaster* embryo. *Elife* **6**(2017).
51. Negre, N. et al. A comprehensive map of insulator elements for the *Drosophila* genome. *PLoS Genet.* **6**, e1000814 (2010).
52. Kyrchanova, O. & Georgiev, P. Chromatin insulators and long-distance interactions in *Drosophila*. *FEBS Lett.* **588**, 8–14 (2014).
53. Chetverina, D. et al. Boundaries of loop domains (insulators): determinants of chromosome form and function in multicellular eukaryotes. *Bioessays* **39** (2017).
54. Lupianez, D. G. et al. Disruptions of topological chromatin domains cause pathogenic rewiring of gene-enhancer interactions. *Cell* **161**, 1012–1025 (2015).
55. Bartman, C. R., Hsu, S. C., Hsiung, C. C., Raj, A. & Blobel, G. A. Enhancer regulation of transcriptional bursting parameters revealed by forced chromatin looping. *Mol. Cell.* **62**, 237–247 (2016).

Author contributions

H.C. and T.G. conceived the main ideas regarding live-cell image generation, processing and analysis. M.F and J.B.J. developed the *homie-eve* system to create quantifiably distinct architectural and transcriptional states. H.C. designed the study to overlap these technologies. H.C., M.F. and J.B.J. designed and generated the transgenic flies. H.C. and L.B. performed the imaging experiments. H.C., L.B., M.L. and T.G. analyzed the data and wrote the manuscript.

Competing interests

The authors declare no competing interests.

Additional information

Supplementary information is available for this paper at https://doi.org/10.1038/s41588-018-0175-z.

Reprints and permissions information is available at www.nature.com/reprints.

Correspondence and requests for materials should be addressed to T.G.

Publisher's note: Springer Nature remains neutral with regard to jurisdictional claims in published maps and institutional affiliations.

Methods

Plasmid construction. The MS2 stem loop cassette is amplified from a previously described *hbb*2-MS2 plasmid[32]. An optimized 24×PP7 sequence is a gift from T. Fukaya[26]. *homie* is amplified from chr2R:9,988,750-9,989,118 (dm6). parS sequence from *Burkholderia* (J2315, chr3:3,440-3,821, GB: AM747722) is a gift from K. Bystricky and F. Paire. MCP and PCP are amplified from Addgene #52985[56]; 3×mTagBFP2 is amplified from Addgene #62449[57]. mKate2 is a gift from J. Ling and a set of three was fused to make 3×mKate2. ParB-GFP is a gift from K. Bystricky and F. Paire. The 256×lacO cassette is cut from addgene #33143[58]. LacI::GFP is amplified from Addgene #40943[59]. All plasmids used for transgenic experiments were made through standard cloning procedures. Plasmid maps and cloning details are available on request.

Transgenic fly generation. To tag endogenous *eve* with MS2 stem loops, a two-step transgenic strategy was used. First, an attP site was integrated into the first intron of *eve* using CRIPSR-mediated homology-directed repair. The homology arms were amplified from the genomic DNA of BDSC #51324, which was used as a genomic source for *nos*-Cas9. The two Cas9 cutting sites are at chr2R:9,979,604-9,979,605 and chr2R:9,980,605-9,980,606 (dm6), respectively. Second, an attB-MS2-lacZ-eve3′UTR plasmid was used to deliver MS2 into the attP site. A genomic source of phiC31 integrase (BDSC #34770) was used for the second injection. The final *eve*-MS2 transformant carries a ~9.5-kb insertion (selection markers) between the *MS2-lacZ-eve* 3′UTR and the downstream *eve* enhancers.

The *eve*-MS2 flies were crossed with a 2×attP genomic landing site at chr2R:9,836,454 (dm6, −142 kb to *eve* promoter[22]) to obtain recombinants that carry *eve*-MS2 and the −142 kb landing site in *cis*. The reporter transgenes were then integrated into the landing site through recombination-mediated cassette exchange using BDSC #34770 as the integrase source.

For the fluorescence-tagged maternal proteins (MCP::3×mTagBFP2, PCP::3×mKate2 and MCP::mCherry), a genomic landing site at 38F1[60] was used. For maternal ParB::eGFP, LacI::GFP and PCP::eGFP, a landing site at 89B8 was used. All microinjections were performed as described previously[61] or through *BestGene* injection service.

FISH. smFISH followed a previously described protocol[62]. Atto labeled probe sets targeting *eve* CDS and the 5′ 1.7 kb of *lacZ* were used. Raw images were processed following Little et al.[63] to identify all cytoplasmic spots and transcription spots. A cytoplasmic unit (CU) that corresponds to the fluorescence intensity of a single cytoplasmic mRNA was calculated. Specifically, a sliding window of 220×220×23 pixels (16.5×16.5×7.4 μm³) was applied to the raw image stack and the total pixel values in the window were plot against the number of cytoplasmic spots found in the window. A linear fit in the range of 0–100 cytoplasmic spots was applied to extract CU for each probe set (Supplementary Fig. 2f, inset). In order to get the number of Pol II in each transcription spot, a cylinder mask (d=13 pixel, h=7 pixel) centered at the brightest pixel in each transcription spot was used to calculate total spot intensities, which were converted using the corresponding CU and probe configuration for the transcribed sequence. Because the *eve-MS2* allele is targeted by only a part of the *eve* probe set, a conversion factor was calculated from the proportion of bound probes. The CU obtained from the full-length *eve* transcripts was then adjusted using this conversion factor to get pol II number on *eve-MS2* from the *eve* channel (y axis in Supplementary Fig. 2f).

Phenotypic scoring. The *homie-evePr-lacZ/CyO* flies or the *λ-evePr-lacZ/CyO* flies were crossed with an isogenic *yw;Sp/CyO* (BDSC #8379) to get *Sp/homie-evePr-lacZ* and *Sp/λ-evePr-lacZ* males. Single males were then crossed with *CyO/Dp(2R)* *eve*⁻ virgins[22] in order to score phenotypic defects in the next generation. Since phenotypic penetrance can be very sensitive to environmental conditions (for example, temperature, humidity, food, etc) and genetic background, our crossing and scoring scheme included controls for all these potentially confounding factors.

Microscopy and imaging conditions. For imaging parS-containing transgenes, virgins carrying three fluorescent protein fusions (*yw*; MCP::3×mTagBFP2/ PCP::3×mKate2; ParB::eGFP/+) were crossed with males carrying the *eve-MS2* allele and the reporter transgene. For the 0-kb co-localization control, virgins carrying three fluorescent protein fusions (*yw*, MCP::3×mTagBFP2/ MCP::mCherry; PCP::eGFP/+) were crossed with males carrying the hbP2-24×MS2PP7-*kni* transgene. For the lacO/LacI control, virgins with three fluorescent protein fusions (*yw*; MCP::3×mTagBFP2/PCP::3×mKate2; LacI::GFP/+) were used. The embryos from the above crosses were manually dechorionated and mounted as described[32]. For bead experiments, 200 nm three-color coated TetraSpec beads were used.

All images were acquired on a Leica SP5 confocal microscope with a Leica oil immersion 63×NA1.44 objective. Three laser lines at 405 nm (0.4 μW), 488 nm (1.1 μW) and 591 nm (0.5 μW) were used to excite the blue, green and red fluorophores, respectively. For bead experiments, we modulated laser powers to get a spectrum of emission signals. Three HyD detectors in photon counting mode were used to collect fluorescence emission spectra. Voxel size for all images was set at 107×107×334 nm³ and the total volume imaged was about 110×27×8 μm³. Frame interval for all time-lapse videos was 30 s, except for the ones shown in

Fig. 1c (15 s). Images were taken at 1,024×256×25 voxels and focused on the posterior half of the embryo, encompassing *eve* stripes 3–7. Embryos that exit mitosis 13 were timed[64]. Imaging started at 20±2 min into nc14 and finished at gastrulation (62±2 min into nc14).

Image processing and data analysis. All image processing and data analysis was performed using MATLAB R2015a, MathWorks.

Nuclear segmentation and tracking. Nuclear segmentation was performed on the difference between the blue and red channels (NLS::MCP::3×mTagBFP2 is enriched in the nuclear compartment while ParB-eGFP is enriched in the cytoplasm): the maximum z-projection of the green channel was subtracted from the blue channel, and the resulting image was subsequently Gaussian blurred (σ=5), binarized (using a local Otsu's threshold at 5×5 μm²) and opened with a disk of diameter d=5 pixels. A watershed transformation was performed on the distance matrix calculated from the binarized image to get the segmentation for each frame, and a nuclear mask was calculated from each segmented region.

Since each frame contains only 70–100 nuclei, we used an exhaustive search for nuclear tracking. Because both the whole embryo and the nuclei might move during imaging, we calculated a local vector that recapitulates the nuclear movement by minimizing cross-correlation between nuclear masks of two consecutive frames. After correcting for movement, we multiplied each nuclear mask at time t to all individual nuclear masks from t+1, and the matching nucleus was selected based on the total pixel value of the product images. All nuclear segmentation and tracking results were scrutinized manually.

Candidate spot identification. We built a candidate spot library for each video. First, raw image stacks from each of the three channels were sharpened using a 3D bandpass filter of size 11×11×7 pixels, which was derived from subtracting a uniform filter from a Gaussian kernel (σ=(1, 1, 0.6) pixel). We treated all local maxima in the filtered image as putative spots, and a cylinder mask with diameter of 13 pixels (1.4 μm) and a height of 7 pixels (2.3 μm) centered at each local maximum was constructed. The size of the mask was determined by the size of the mega-spot images (Supplementary Fig. 3e-h) and covered >97% of signals emitted from the chromatin foci. Therein we summed up all pixels inside the mask to get the intensity of each putative spot. Finally, for each nucleus at each time point, an intensity threshold was chosen to select candidate spots from the local maxima, in such a way that the maximum number of candidate spots in the nucleus was less than 20. In the subsequent steps, we filtered the candidate spot library using information on nuclear lineage, spot tracking and the relative location of spot pairs.

Spot tracking. The intensity-weighted centroid was calculated within the mask of each candidate spot, and the *FracShift* algorithm[65] was applied to find the sub-pixel center for each spot. No sub-pixel bias was observed after ten *FracShift* iterations. We did spot tracking in each nuclear lineage. For each lineage, candidate spots located in the corresponding nuclear region (from the nuclear segmentation results) were used for tracking. Spot tracking was performed in three steps: a pre-tracking step, a gap-filling step and a Bayes filtering step.

Step I: For the pre-tracking step, we tracked the two brightest candidate spots in each nucleus. The maximally allowable displacement of spots from the consecutive frames was determined from the MSD at Δt=30 s (1 frame, see "MSD analysis" section below and Supplementary Fig. 4d) and the measurement error (e_L, see "Estimating localization errors" section below and Supplementary Fig. 3a–d) for each dimension. Specifically, for each candidate spot at time t, a search zone of size $3\times(\sqrt{\text{MSD}/2}+e_L)$ was set up around the spot center. After correcting for nuclear shift, a candidate spot in the searching zone at time t+1 was recorded, and other candidate spots were discarded. In the <1% of cases where there was more than one candidate spot in the search zone, the brightest one was chosen. Finally, all traces shorter than 2 min are treated as false positives and discarded. These false positive traces are usually clusters of completed mRNAs that are undergoing nuclear export. All tracking was performed on videos of 35 min length (22–58 min in n.c.14). The three channels (MS2, PP7 and parS) were tracked independently. Pre-tracking results from all channels were compiled according to nuclear lineages.

Step II: After collecting the pre-tracking results, we analyzed for each channel (1) the distribution of spot axial positions, (2) the distribution of spot intensities, (3) the distribution of displacement vectors, and additionally for the blue (*eve-MS2*) channel, and (4) the distribution of spot anterior-posterior positions. We then implemented a Dijkstra algorithm[66] to find the minimal path that fills the gaps in the pre-tracking results. Specifically, using the distributions described previously, we calculated a cost function (log likelihood) for each link that connects any two candidate spots from two consecutive frames and constructed the set of links that minimized the sum of the costs across the gap. At the end of this gap-filling step, we obtained one tracked spot for each nucleus at each time point.

Step III: Finally, we filtered these tracked spots using a Bayes binary filter. First, a false positive data set (FP) is constructed by re-tracking the candidate spot library after removing spots that were previously tracked. The pre-tracking result from Step I was used as the true positive set (TP). For each spot obtained from Step II, we then used the information (info) of its location, intensity, the displacement from the previous frame and the displacement toward the next frame to obtain

likelihood $P(\text{info}|\text{FP})$ and $P(\text{info}|\text{TP})$, respectively. Next, we calculated the priors $P(\text{FP})$ and $P(\text{TP})$ by fitting a two-component Gaussian mixture model for the vectors that connects the tracked blue and green spots in the same nucleus. Finally, we obtained the posterior probability $P(\text{TP}|\text{info})$ and used a cutoff that maximizes the Matthews correlation coefficient to filter false positive spots. The sensitivity of the filter ranged from 96.2% to 99.1%, and the false discovery rate was less than 1%.

Calibrating chromatic aberrations. Chromatic aberration was corrected to measure distance between spots of different colors. The calibration was data-driven and internally controlled. We assumed that the vector between a spot pair of two different colors in the same nucleus has a zero mean in each dimension. An MS2 spot (blue), for instance, has the same probability of appearing on top of the associating parS spot (green) as the probability of appearing below it, and the distribution is symmetric around zero. We performed additional control experiments to verify this assumption (see below).

We pooled raw instantaneous spot-pair distances from all nuclei at all time points in all available embryos and analyzed the raw distances as a function of the spot-pair positions in the image field of view (for example, Supplementary Fig. 3b shows the blue-green distance in the x-direction as a function of the x-position in the image of view). We applied a multivariate normal regression model ($A_i = p_i\beta + e_i$, $i = x, y, z$) in order to get the correction matrix β, where A_i is the 3D response vector for the chromatic aberration, p_i is the spot position with a constant term, and e_i is a normally distributed error. For each spot pair, chromatic aberration was calculated using β, and the calibrated distances were used in further analysis. The correction matrix was calculated on a weekly basis, using all embryos imaged over the week (embryo number ranging from 12 to 25, usually of the same genotype).

To test the validity of the zero mean assumption described previously, we undertook two control experiments. First, we imaged our co-localization control embryos in which blue, green and red fluorescent proteins co-localized within a genomic distance of 2 kb (Supplementary Fig. 3a). Second, we made videos of the 200 nm three-color *TetraSpec* beads. These experiments were performed during the same week and under the same optical settings as for the *parS-homie-evePr-PP7* embryos, and the images were analyzed using the same code pipeline. Next, we applied the same calibration method to obtain the correction matrix for the control embryos or beads. There was no significant difference between the fitting parameters obtained from the *parS-homie-evePr-PP7* embryos and those from the control embryos or beads (Supplementary Fig. 3b). Specifically, applying the correction matrix derived from the control embryos on the experimental embryos introduced <0.6% difference in the calibrated distances.

Estimating localization errors. To estimate the precision in our distance measurement, we used the three-color control embryos described above. Briefly, the standard deviation (s.d.) from the fitted line (Supplementary Fig. 3b, middle), which is the mean after chromatic correction, represents the localization error (e_L). For example, for the distance between the MS2 (blue) and parS (green) spots, the s.d.s for the lateral and axial directions are 75 nm and 150 nm, respectively (Supplementary Fig. 3c). These errors were subtracted in the calculations of time or population-averaged r.m.s. distances (see "Calculating r.m.s. distances" section below).

We then assessed whether these localization errors result from optics or from the dynamic properties of our live embryos. From the beads videos we measured lateral and axial errors of 20 nm and 50 nm, respectively (Supplementary Fig. 3c). The differences in the measurement errors between embryos and beads were not due to differences in photon counts (Supplementary Fig. 3d). We conclude that approximately two-thirds of our localization errors were derived from the properties of the live system. At least two factors might contribute to the increased errors we observed in the embryo. First, the nuclei were imaged during S or G2 phase, and individual transcription spots actually represent two sister chromatids. Second, each z-slice takes ~1 s, and the expected MSD is ~0.1 μm² from the extrapolation of our MSD analysis. As a result, the movement of the spots between two consecutive z-stacks introduces 'motion blur', which leads to increased localization error. Since the *parS-homie-eve-PP7* embryos are expected to share the same biological and optical properties as the three-color control embryos, we assume the same localization errors.

Calculating r.m.s. distances. We report time- or population-averaged r.m.s. distances between the MS2 (blue) and the parS (green) spot pairs. For time-averaged r.m.s. distances, instantaneous distances measured at different time points in the same nucleus were averaged. We analyzed the distribution of r.m.s. distances calculated at different time scales, either for the complete time trace (Supplementary Fig. 6) or for a short time window (5 min, Fig. 3a) in order to characterize topological transitions occurring at the relevant time scales. We further classified all r.m.s. distances into two groups (Red-ON and Red-OFF) according to the presence or absence of the red signal (*PP7* transcription). For r.m.s. distances obtained from the complete traces, Red-OFF r.m.s. distances were calculated from traces that never show PP7 transcription, while Red-ON r.m.s. distances were calculated from the part of the traces that displayed PP7 activity (Supplementary Fig. 6). For r.m.s. distances obtained from short sliding time windows, Red-OFF r.m.s. distances were calculated from traces that never showed

PP7 transcription, and Red-ON r.m.s. distances were calculated from traces that displayed PP7 activity at all time points across the window (Fig. 3a).

We also calculated population-averaged r.m.s. distances (Fig. 2, Fig. 3b–d, Supplementary Fig. 8k) for a group of nuclei that shared the same temporal or spatial register. For example, we aligned all traces with Red-OFF to Red-ON transitions and calculated the r.m.s. distances from nuclei aligned at the same time relative to the initiation of PP7 transcription (Fig. 2a). Similarly, we calculated r.m.s. distances for all nuclei classified as being in the same topological state (Fig. 3b–d, Supplementary Fig. 8k).

Since the measurement errors (e_i) described in the previous section and spot pair distances did not seem to be correlated, we reported an error-corrected r.m.s.$_{\text{corr}}$, obtained by subtracting the errors from the raw r.m.s. distances: r.m.s.$_{\text{corr}}^2$ = r.m.s.$^2 - \Sigma_{i=(dx,dy,dz)} e_i^2 = \Sigma_{i=(dx,dy,dz)} \langle i + e_i \rangle^2 - \Sigma_{i=(dx,dy,dz)} e_i^2$, where i is the actual blue-green (MS2-parS) distance in each dimension and e_i is the localization error in the corresponding dimension, which is the s.d. obtained from the three-color control (Supplementary Fig. 3c).

Gaussian mixture fits. The probability distribution functions of r.m.s. distances (except for the λ control in Fig. 3c) were modeled with two-component Gaussian mixtures with five parameters: two means (μ_1 and μ_2) and s.d.s (σ_1 and σ_2) for the two Gaussians and the proportion (p) of the components. Maximum likelihood estimates were performed using MATLAB's *mle* function. The fitting results were robust to the choice of initial values, and convergence was always reached after 250 iterations. For the *parS-homie-evePr-PP7* embryos, the Gaussian component with the smaller mean is composed of two populations.

Time trace alignment. Time series of *PP7* activities were aligned with respect to 1) the initiation of *PP7* transcription, that is, the first time point at which nascent *PP7* transcripts (red spots) could be detected, or 2) the termination of *PP7* transcription, that is, the last time point at which *PP7* transcripts could be identified; 90% of nuclei with *PP7* activities contained single *PP7* activity traces. For the other 10% of nuclei in which there are two *PP7* activity traces, we aligned the initiation of the first trace or the termination of the second. There were cases where *eve-MS2* and *PP7* transcription started at the same time, presumably because *homie-homie* pairing occurred before *eve* enhancers started to function. Therefore, for the initiation analysis, we only aligned *PP7* activity traces where *eve-MS2* transcription appeared at least 3 min before *PP7* transcription was activated. Similarly, for the termination analysis, we only aligned *PP7* activity traces where *eve-MS2* transcription lasted for at least 3 min after *PP7* transcription ceased.

MSD analysis. We analyzed the relative motion between two associated spots (for example, MS2 and parS) by computing the time-averaged mean squared displacement (MSD), that is, the mean squared change in distances, between a specific spot pair over all time points separated by time interval Δt (Supplementary Fig. 4d). We computed an embryo-averaged MSD and a population-averaged MSD by pooling all spot pairs in an embryo and all spot pairs in a population of embryos, respectively. The embryo-averaged and population-averaged 3D MSDs were fit to a model for 3D anomalous diffusion, that is, MSD = $6D(\Delta t)^\alpha$ with an anomalous diffusion coefficient D and a scaling factor α that were extracted. Non-linear least-squares fits were performed for $\Delta t < 4$ min.

Classification of instantaneous topological states. Because of the fast chromatin motion ($D = 0.04\,\mu m^2\,s^{-0.24}$, Fig. 1e, Supplementary Fig. 4d) and the relatively small confinement of the enhancer–promoter locus (~1 μm for the open state), distributions of the instantaneous enhancer–promoter distance for the open state and the *homie-homie* paired state overlapped significantly, which hindered the characterization of the instantaneous topological state of the enhancer–promoter locus. We therefore took advantage of the continuity of live imaging and calculated the velocity of the relative enhancer–promoter movement (displacement across one frame) at each time point (Supplementary Fig. 8a,b). Since the time scale of topological state transitions seems to be at least one order of magnitude slower than the time resolution of our live imaging (which is validated by our kinetic model), the velocities provide extra information for identifying the instantaneous topological state.

We therefore used a binary classifier to classify each enhancer–promoter locus at each time point regarding its topological state, either open (O) or paired (P). We applied one training sample for each of the two states. For the open state, we used time series traces obtained from the *parS-λ-evePr-PP7* embryos, which presumably were composed solely of the open state. For the paired state, we used all traces where PP7 transcription occurred, considering that physical proximity is required for promoter activity so that time series traces accompanied by PP7 activity were exclusively in the paired state. For each training sample, we modeled the joint distribution of the distance vector and the velocity vectors as a multivariate Gaussian (Supplementary Fig. 8c–j). There is a negative correlation (−0.32, Pearson correlation coefficient) between velocities measured in two consecutive frames (Supplementary Fig. 8g–j), which is consistent with the strong sub-diffusive behavior we observed from the MSD analysis ($\alpha = 0.24$, Supplementary Fig. 4d).

Using the distance and the velocity information (Data), we calculated the likelihood $P(\text{Data}|\text{O-state})$ and $P(\text{Data}|\text{P-state})$ from the two trained joint

distributions, respectively. Furthermore, we calculated the priors P(P-state) and P(O-state), for each developmental time point, by pooling data from all embryos. Specifically, we used a time window (5 min) centered at the specific time point and calculated the r.m.s. distance for each nucleus. The distribution of these r.m.s. distances was modeled as a two-component Gaussian mixture, and the proportion of the Gaussian component with the smaller mean was used as prior P(P-state) for this developmental time point.

The posterior probability P(P-state|Data) was then calculated according to Bayes rule. Finally, we estimated the errors (specificity and sensitivity) of our classifier from the two training samples, and a posterior probability cutoff that maximizes the Matthews correlation coefficient was used for state calling.

Modeling topological state transitions and MCMC Inference of kinetic parameters. We used a set of first-order reactions to model the transitions between the three topological states (Supplementary Fig. 9a). Based on the finding that physical proximity is required for transcriptional activation, we built a model such that P_{on} occurs only after P_{off} is established. Assuming that the parameters f_1 and b_1 are the same for both the *parS-homie-evePr-PP7* and the *parS-homie-noPr-PP7* constructs, we also used the O_{off} time series from the latter to constrain our parameter inference.

To infer the kinetic parameters, we used Metropolis–Hastings algorithm to perform MCMC. Specifically, given a parameter set:

$$\theta = \bigcup_{k=1,2\ldots,8} \{\theta_k\}$$
$$= \{f_1, b_1, f_2, b_2, b_3, F_{ini}(O_{off}, homie), F_{ini}(P_{on}, homie), F_{ini}(O_{off}, noPrmt)\}$$

where the three F_{ini} are the initial conditions for the indicated states and genotype, we used time series $D = \bigcup_{i,j} \{F_j(t_i), \sigma_j^2(t_i)\}$ to calculate the likelihood:

$$P(D \mid \theta) = \prod_{i,j} N\left(f_j(t_i) \mid \theta, \ \mu_{i,j} = F_j(t_i), \sigma_j^2(t_i)\right)$$

where $f_j(t_i) | \theta$ is solved numerically from the coupled ordinary differential equations (Supplementary Fig. 9a) with MATLAB ode45. $F_{j=1,2,3}$ corresponds to the measured time series of the fraction of the O_{off} state for *parS-homie-evePr-PP7*, the fraction of the P_{on} state for *parS-homie-evePr-PP7*, and the fraction of the O_{off} state for *parS-homie-noPr-PP7*, respectively, and $i = 1, 2,\ldots, T$ are the developmental time points from 25 to 55 min in nuclear cycle 14.

Using prior $\pi_0(\theta) = \prod_k (1/\theta_k)$ and a log-normal proposal distribution:

$$J(\theta^* \mid \theta) = \log \mathcal{N}(\log(\theta), \ \Sigma)$$

we generated a Markov chain to sample posterior distributions of the kinetic parameters with acceptance probability:

$$\alpha(\theta^*, \theta) = \min\left(1, \frac{P(D \mid \theta^*)\pi_0(\theta^*)J(\theta \mid \theta^*)}{P(D \mid \theta)\pi_0(\theta)J(\theta^* \mid \theta)}\right)$$
$$= \min\left(1, \prod_{i,j} \mathcal{N}(F_j(t_i)|\theta^*, \sigma^2(t_i)) \prod_{i,j} \mathcal{N}(F_j(t_i)|\theta, \sigma^2(t_i))^{-1}\right)$$

All simulated chains converged after 5,000 iterations, and we used 90,000 stationary samples to represent the posterior distributions of the kinetic parameters (Supplementary Fig. 9c–g).

Transcriptional activity measurements. Transcriptional activity was measured as the sum of the pixel intensities in the spot mask ($d = 1.4\,\mu m$, $h = 2.3\,\mu m$). For aligned *PP7* activity traces (Fig. 2, Supplementary Fig. 5) where *PP7* was not active (Red-OFF part), a mask around the parS spot (green) in the same nucleus was made.

The mask was allowed to shift within the range defined by the mean parS-PP7 (green-red) distance. The maximal integrated intensity in the red channel was used as the *PP7* activity.

Endogenous eve activity comparison. For each trace with *PP7* activity, we integrated *eve-MS2* activity in the same nucleus to get *eve-MS2* activity while *PP7* transcription is active (eve|Red-ON, Fig. 4a, *x* axis). Only nuclei with *PP7* activity lasting longer than 12 min were used. To obtain the control, which is the *eve-MS2* activity while PP7 transcription is not active (eve|Red-OFF, Fig. 4a, *y* axis), we calculated the mean of the integrated *eve-MS2* activities in the neighboring nuclei where *PP7* was not transcribed. Neighborhood is defined as nuclei within a 20 μm anterior-posterior bin centered at the nucleus displaying *PP7* activity. The time interval for *eve-MS2* activity integration is the same as for the *PP7* expressing nucleus. The time-averaged integrated intensity is shown in Fig. 4a.

Statistical analysis. Two-tailed Wilcoxon rank sum tests were performed to compare enhancer–promoter distances in different topological states. One-tailed Fisher's exact tests were performed to test for enhanced penetrance of the phenotypic defects associated with the *homie* transgenes. MCMC inference of the kinetics parameters is described in Image processing and data analysis. Representative images/videos were replicated in at least three independent experiments, as indicated in the relevant figure legends.

Reporting Summary. Further information on experimental design is available in the Nature Research Reporting Summary linked to this article.

Code availability. Custom codes (MATLAB) used for image processing and data analysis can be made available on request. All details of algorithms are described in the Methods and references cited therein.

Data availability. Raw spot localization data are provided as Supplementary Data 1. Raw videos are available on request.

References

56. Wu, B., Chen, J. & Singer, R. H. Background free imaging of single mRNAs in live cells using split fluorescent proteins. *Sci. Rep.* **4**, 3615 (2014).
57. Sladitschek, H. L. & Neveu, P. A. MXS-chaining: a highly efficient cloning platform for imaging and flow cytometry approaches in mammalian systems. *PLoS One* **10**, e0124958 (2015).
58. Vodala, S., Abruzzi, K. C. & Rosbash, M. The nuclear exosome and adenylation regulate posttranscriptional tethering of yeast GAL genes to the nuclear periphery. *Mol. Cell* **31**, 104–113 (2008).
59. Dubarry, M., Loiodice, I., Chen, C. L., Thermes, C. & Taddei, A. Tight protein-DNA interactions favor gene silencing. *Genes Dev.* **25**, 1365–1370 (2011).
60. Bateman, J. R., Lee, A. M. & Wu, C. T. Site-specific transformation of *Drosophila* via phiC31 integrase-mediated cassette exchange. *Genetics* **173**, 769–777 (2006).
61. Small, S. In vivo analysis of lacZ fusion genes in transgenic *Drosophila melanogaster*. *Methods Enzymol.* **326**, 146–159 (2000).
62. Little, S. C., Tkacik, G., Kneeland, T. B., Wieschaus, E. F. & Gregor, T. The formation of the Bicoid morphogen gradient requires protein movement from anteriorly localized mRNA. *PLoS Biol.* **9**, e1000596 (2011).
63. Little, S. C., Tikhonov, M. & Gregor, T. Precise developmental gene expression arises from globally stochastic transcriptional activity. *Cell* **154**, 789–800 (2013).
64. Dubuis, J. O., Samanta, R. & Gregor, T. Accurate measurements of dynamics and reproducibility in small genetic networks. *Mol. Syst. Biol.* **9**, 639 (2013).
65. Gao, Y. & Kilfoil, M. L. Accurate detection and complete tracking of large populations of features in three dimensions. *Opt. Express* **17**, 4685–4704 (2009).
66. Dijkstra, E. W. A note on two problems in connexion with graphs. *Numer. Math.* **1**, 269–271 (1959).

Dynamic interplay between enhancer–promoter topology and gene activity

Hongtao Chen[1], Michal Levo[1], Lev Barinov[2], Miki Fujioka[3], James B. Jaynes [ID][3] and Thomas Gregor [ID][1,4,5]*

[1]Lewis-Sigler Institute for Integrative Genomics, Princeton University, Princeton, NJ, USA. [2]Department of Molecular Biology, Princeton University, Princeton, NJ, USA. [3]Department of Biochemistry and Molecular Biology, and the Kimmel Cancer Center, Thomas Jefferson University, Philadelphia, PA, USA. [4]Joseph Henry Laboratories of Physics, Princeton University, Princeton, NJ, USA. [5]Department of Developmental and Stem Cell Biology, Institut Pasteur, Paris, France. *e-mail: tg2@princeton.edu
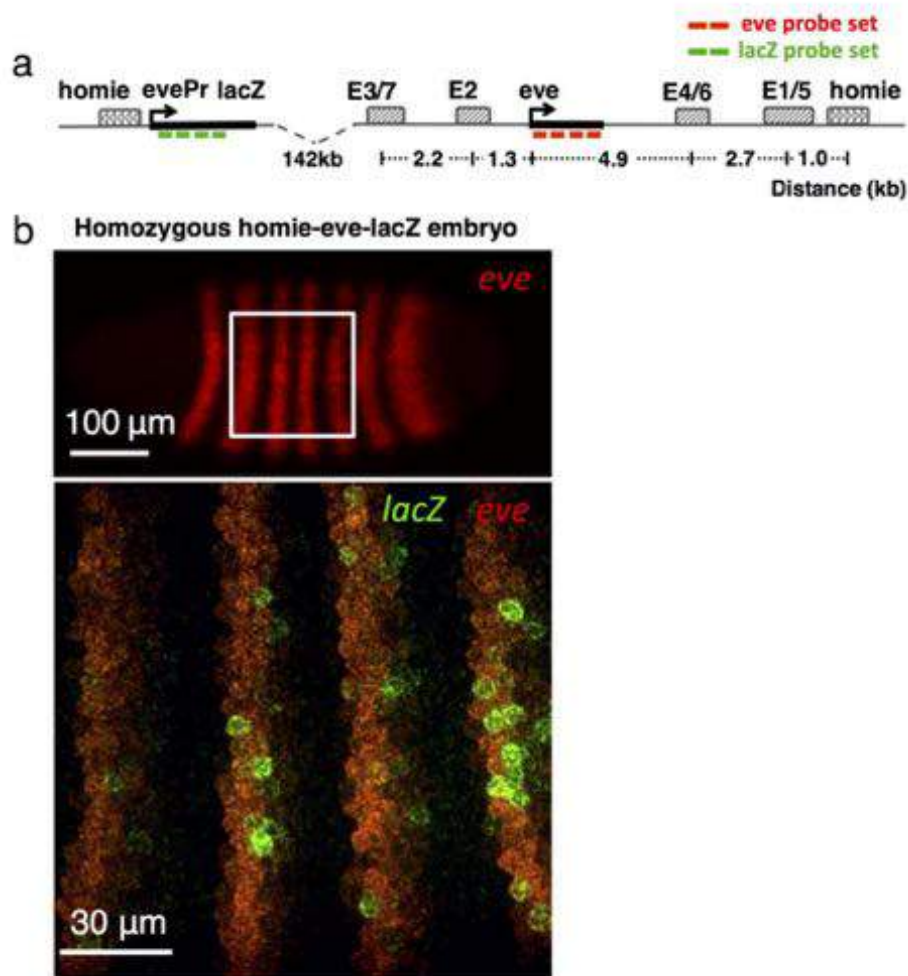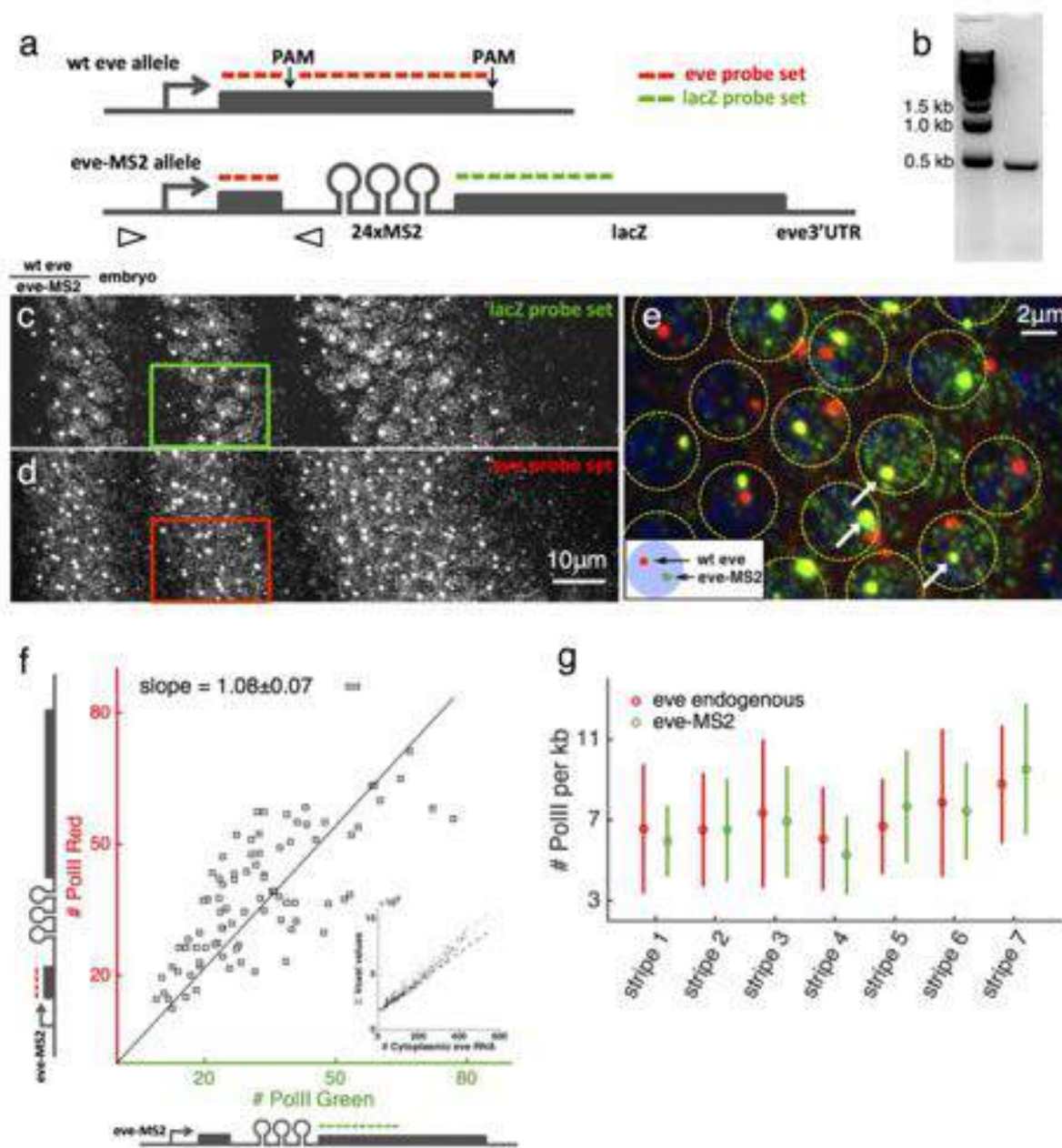
Supplementary Figure 1

FISH reveals *eve* enhancer-dependent expression of a reporter gene located 142 kb upstream of the endogenous *eve* locus.

a, Genomic design of a synthetic long-range enhancer–promoter interaction. An ectopic *homie* insulator sequence with an *eve* promoter driving *lacZ* is integrated at ~142 kb upstream of the *eve* locus. Embryos homozygous for this construct are hybridized with single-molecule FISH probes to label endogenous *eve* (red) and *lacZ* (green) mRNA. **b**, Top, surface view of a 2.5-h-old *Drosophila* embryo hybridized with *eve*-atto633 probes. Anterior is to the left. Bottom, *z*-stack projection of the marked region in the top panel. *LacZ* activity (labeled with *lacZ*-atto565 probes) only occurs sporadically within the limits of the *eve* pattern (red). This *lacZ* pattern appears in all 13 embryos imaged (2–3 h old) and a representative sample is shown here.
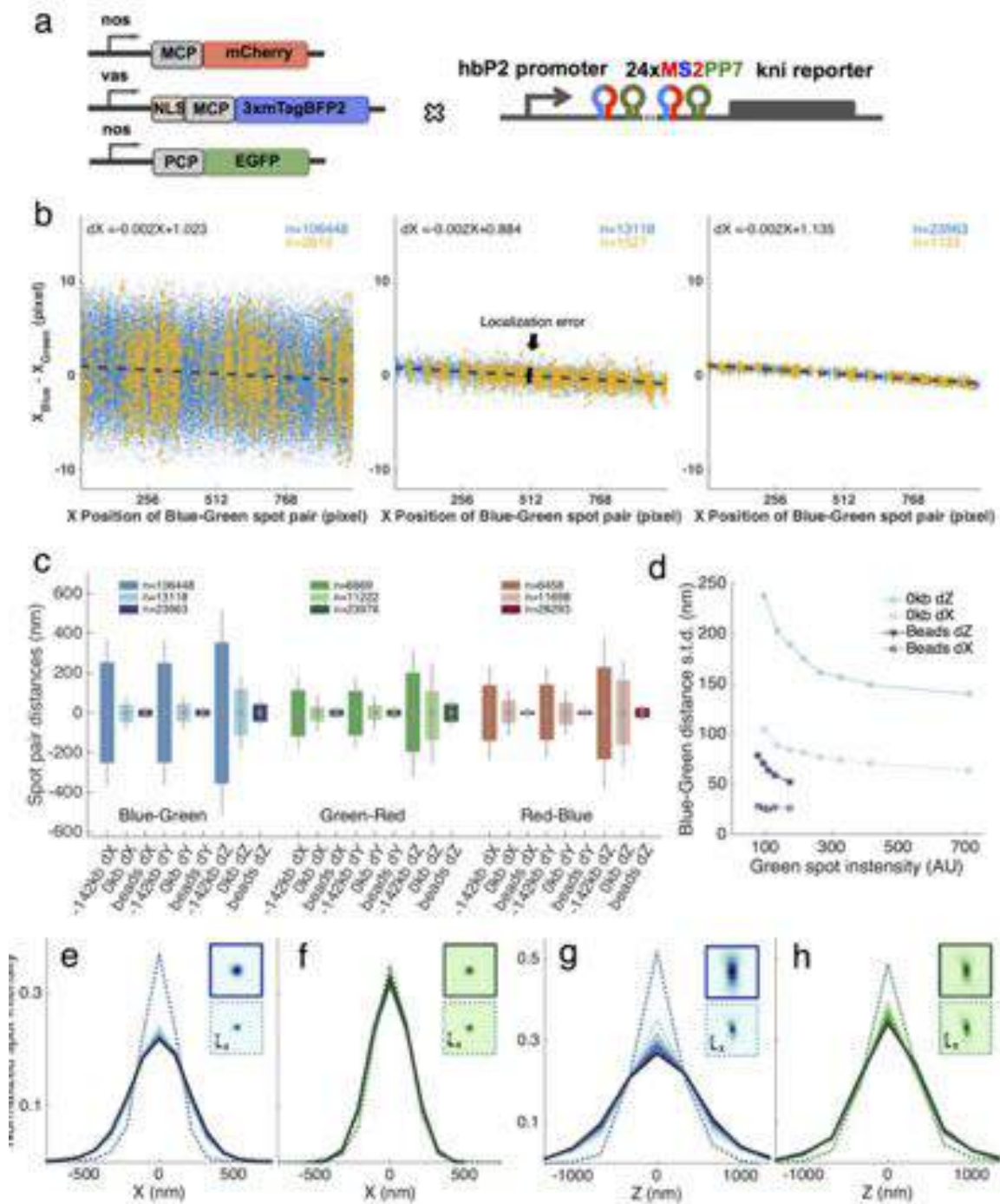
Supplementary Figure 2

The *eve*-MS2 allele recapitulates the expression pattern and transcriptional activity of the endogenous *eve* gene.

a, Editing the endogenous *eve* locus (top) to obtain the *eve*-MS2 allele (bottom). Arrowheads indicate primers for PCR genotyping. Green and red lines mark sequences targeted by smFISH probes (*lacZ*-atto565 and *eve*-atto633, respectively). Loci are not drawn to scale. **b**, Genotyping the *eve*-MS2 allele. The PCR result from a single fly carrying the *eve*-MS2 allele is shown with DNA ladder. The 466-bo band was verified by sequencing. Primers are shown in **a**. **c–g**, smFISH quantification of the transcriptional activity of the *eve*-MS2 allele from a representative embryo at ~45 min into nc14. Maximum *z* projections are shown for the *lacZ*-atto565 channel (**c**) and the *eve*-atto633 channel (**d**) of an *eve*-MS2/*eve*⁺ embryo. *eve* stripes 5 to 7 (from left to right) are shown. **e**, Magnified view of the square in **c** and **d**. Nuclear regions are marked with yellow dashed lines. Arrows indicate examples of *eve*-MS2 transcription loci that are labeled by both probes. **f**, Cytoplasmic spots and active transcription spots were identified by image analysis routines (Methods). A cytoplasmic unit (CU) that corresponds to the fluorescent intensity of a single cytoplasmic mRNA is extracted. The panel shows the number of RNA polymerase II (PolII) on the *eve*-MS2 loci from 93 nuclei in which a transcription spot in the *eve*-atto633 channel was

observed at the *eve*-MS2 locus. The PolII numbers are inferred from either the CU derived from *lacZ*-atto565 (*x* axis) or eve-atto633 (*y* axis) measurements. The inset shows the calculation of cytoplasmic unit for *eve*. Specifically, a sliding window of 220 × 220 × 23 pixels (16.5 × 16.5 × 7.4 μm^3) is applied to the raw image stack (**c** and **d**) and the total pixel values in the window are plotted against the number of cytoplasmic spots found in the window. A linear fit in the range of 0–100 cytoplasmic spots is applied to extract CU for each probe set. **g**, Comparison of the PolII number on the *eve*-MS2 locus and on the endogenous *eve* locus (mean ± s.d.). Note that the numbers reported in **f** and **g** are for two sister chromatids. The number of nuclei analyzed for stripes 1 to 7 was 25, 28, 24, 23, 25, 27 and 54, respectively. Analysis performed on other embryos (*n* = 3) imaged at different stages in nc14 also showed no significant difference in PolII numbers on the *eve*-MS2 locus and the endogenous *eve* locus.
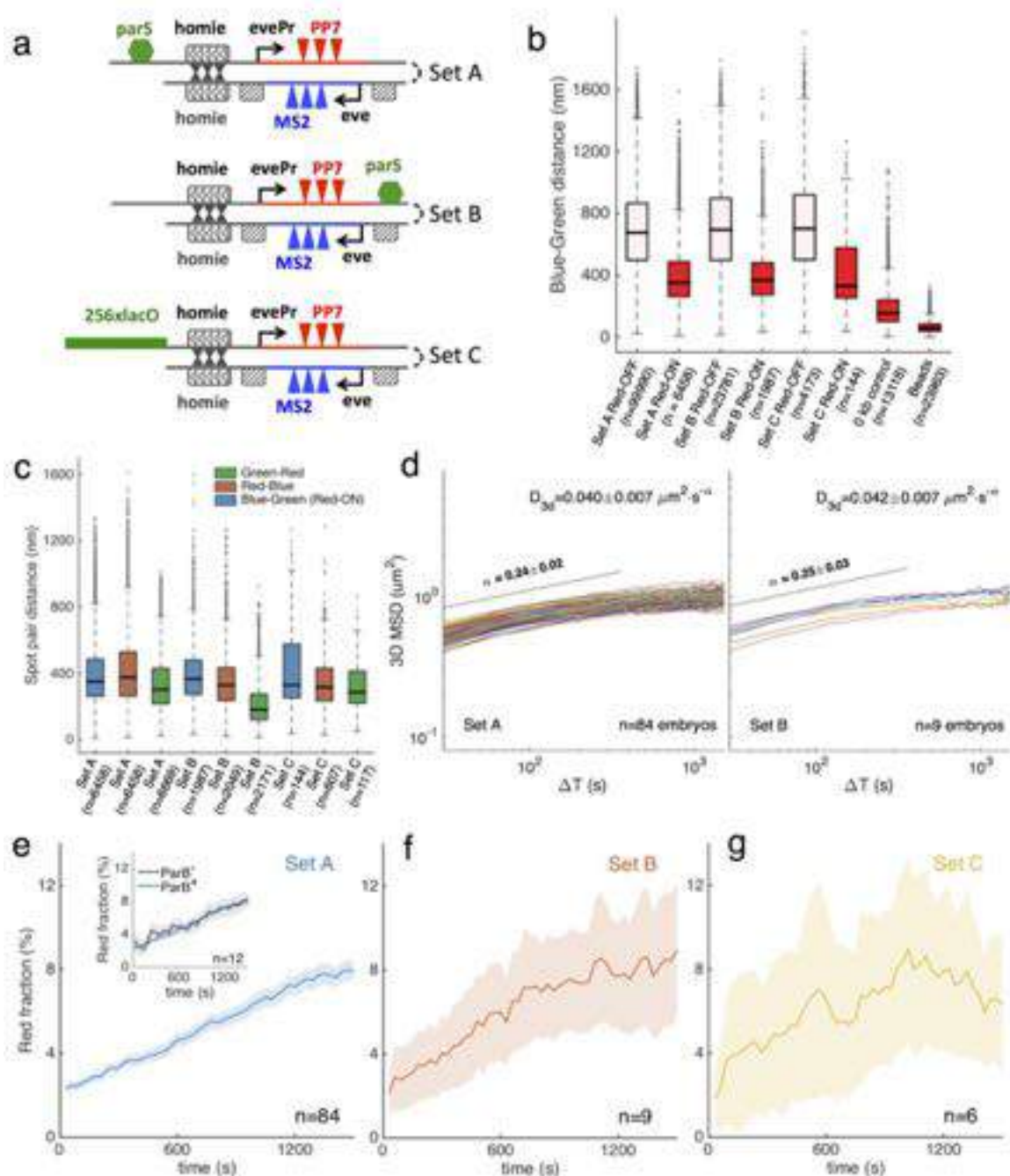
Supplementary Figure 3

Spot localization precision and measurement error.

a, Genetic design of a transgene that colocalizes all three reporter systems. MS2 and PP7 stem loops are alternated and repeated 24 times. A *knirps* (*kni*) reporter gene, which includes the *kni* CDS (with the start codon removed) and 3′ UTR, is driven by a hunchback P2 (*hbP2*) promoter, resulting in expression in all nuclei located in the anterior 10–45% of the embryo. **b,** Analysis of chromatic aberration and localization error (Methods). Panels show the linear distance (along the *x* coordinate only) for each blue-green spot pair as a function of the pair's *x* position for *eve*-MS2 embryos carrying the *parS-homie-eve-PP7* transgene (left, *n* = 34 embryos), embryos

carrying the three-color colocalization transgene from **a** (middle, $n = 9$ embryos), and TetraSpec beads (right, $n = 5$ independent data sets), respectively. Blue data points are for all spot pairs at all time frames for all embryos analyzed. Yellow data points are from one of the embryos (or one set of experiment for the beads). Linear fits in each panel report on the chromatic aberrations between blue and green spots in the x direction. As slopes and intercepts for the different samples show no significant differences, chromatic aberrations can be corrected for each individual embryo dataset internally. **c**, Summary of the distributions of spot pair distances (after chromatic aberration correction) for the three configurations in **b**. Each direction (x, y, and z) is shown for each color combination. For example, for the blue-green (MS2-parS) distances in the x direction, the s.d. of the *parS-homie-eve-PP7* transgene (labeled –142 kb) corresponds to the solid black bar shown in the left panel of **b**. Spot localization errors are estimated from the s.d. measured with the three-color colocalization control embryos (labeled 0 kb). Center values, means; solid lines, s.d.; bars, 25–75% quantiles. **d**, Dependence of localization precision on signal intensities. Since localization precision scales directly with the square root of the number of photons, we can assess localization error of the three-color colocalization control embryos from the localization error measured with immobilized beads of similar fluorescent intensity values (photon counts). Thus, differences in y-axis offset are not due to differences in photon counts but are due to 'motion blurring' of the moving spot during acquisition, which amounts to about two-thirds of the total localization. The remaining one-third (corresponding to the error obtained from immobile beads) stems from optical measurement noise and our analysis pipeline. **e**–**h**, Optical characterization of nascent transcription sites and parS foci. For each fluorescent channel, all identified fluorescent spots are classified into eight groups according to their raw intensities. A 'super-spot' for each group is obtained by aligning all spots of a group with the brightest pixel at the center of a 25 × 25 × 13 voxel region of interest and by taking the average intensity per voxel in that region over all spots. The intensity profiles along the x (**e**,**f**) and z (**g**,**h**) cross-sections for the blue MS2 super-spot (**e**,**g**) and green parS super-spot (**f**,**h**) are plotted (darker curves represent brighter spots). Dashed lines are from equivalent measurements of TetraSpec beads. Images of the super-spots for the brightest blue (MS2; **e**,**g**) or green (parS; **f**,**h**) spots (top) and for the beads (bottom) are shown as panel insets.
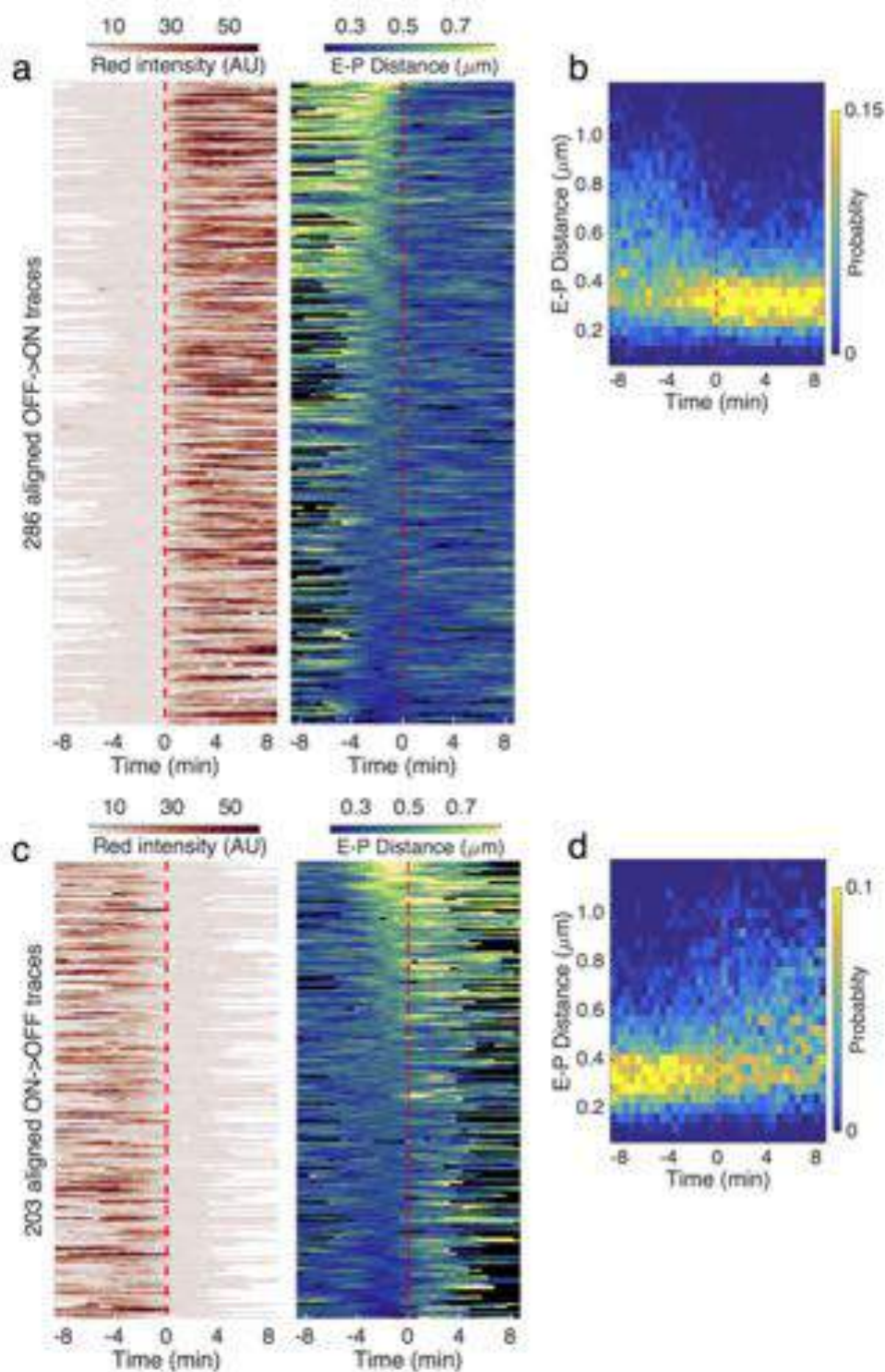
Supplementary Figure 4

Different genomic labeling approaches report on similar chromatin dynamics and transcription kinetics.

a, Three methods of labeling genomic loci. **b**, The measured blue-green (MS2-parS) distances are not sensitive to labeling approach. The box plot shows the distributions of the instantaneous distance between spot pairs in the same nuclei. Distances shown are after chromatic aberration corrections. For all three genomic settings, the MS2-parS (blue-green) distances showed no significant differences (one-way Kruskal–Wallis test on individual embryo mean distances, n = 34, 9 and 6 embryos for sets A, B and C, respectively). This was observed regardless of the absence (Red-OFF, P = 0.17, χ^2 = 4.3, d.f.=50) or presence (Red-ON, P = 0.60, χ^2 = 1.04, d.f. = 49) of *PP7* activity. Center values, medians; boxes, interquantile ranges (25–75% quantiles); whiskers, 1.5 times the interquantile range. The 0 kb control is the *hbP2-MS2PP7-kni* embryo described in Supplementary Fig. 3. **c**, The distances between spot pairs reflect their

genomic arrangement. Distributions of the instantaneous distance between spot pairs are plotted. Box-and-whisker plots are as described in **b**. Distances shown are after chromatic aberration corrections. Note that the parS-PP7 (green-red) distance is significantly shorter when the parS tag is located at the 3′ side of the *PP7* reporter ($P = 4.5 \times 10^{-6}$, two-tailed Wilcoxon rank-sum test). **d**, Mean square displacement (MSD) plots for set A and set B. Each MSD trace is a result of the population ensemble of all nuclei in a single embryo (embryo-averaged MSD; Methods). Results from the two genomic settings display subdiffusive characteristics with a scaling power of ~0.24, and their anomalous diffusion coefficients show no significant difference (two-tailed Student's *t* test, $P = 0.87$, $t = -0.1534$, d.f. = 90; linear fits with mean ± s.d. across embryos). **e–g**, Transcriptional activation of *eve-PP7* is not affected by labeling approach. The fraction of *eve*-MS2-expressing nuclei that also contain active PP7 (mean ± SE) is plotted as a function of time for three genomic settings. It seems that neither the presence nor the location of the parS tag interferes with either enhancer action or transcriptional activation. This is consistent with the hypothesis that the ParB-DNA complex is formed from specific ParB-parS nucleation sites followed by stochastic binding and trapping.
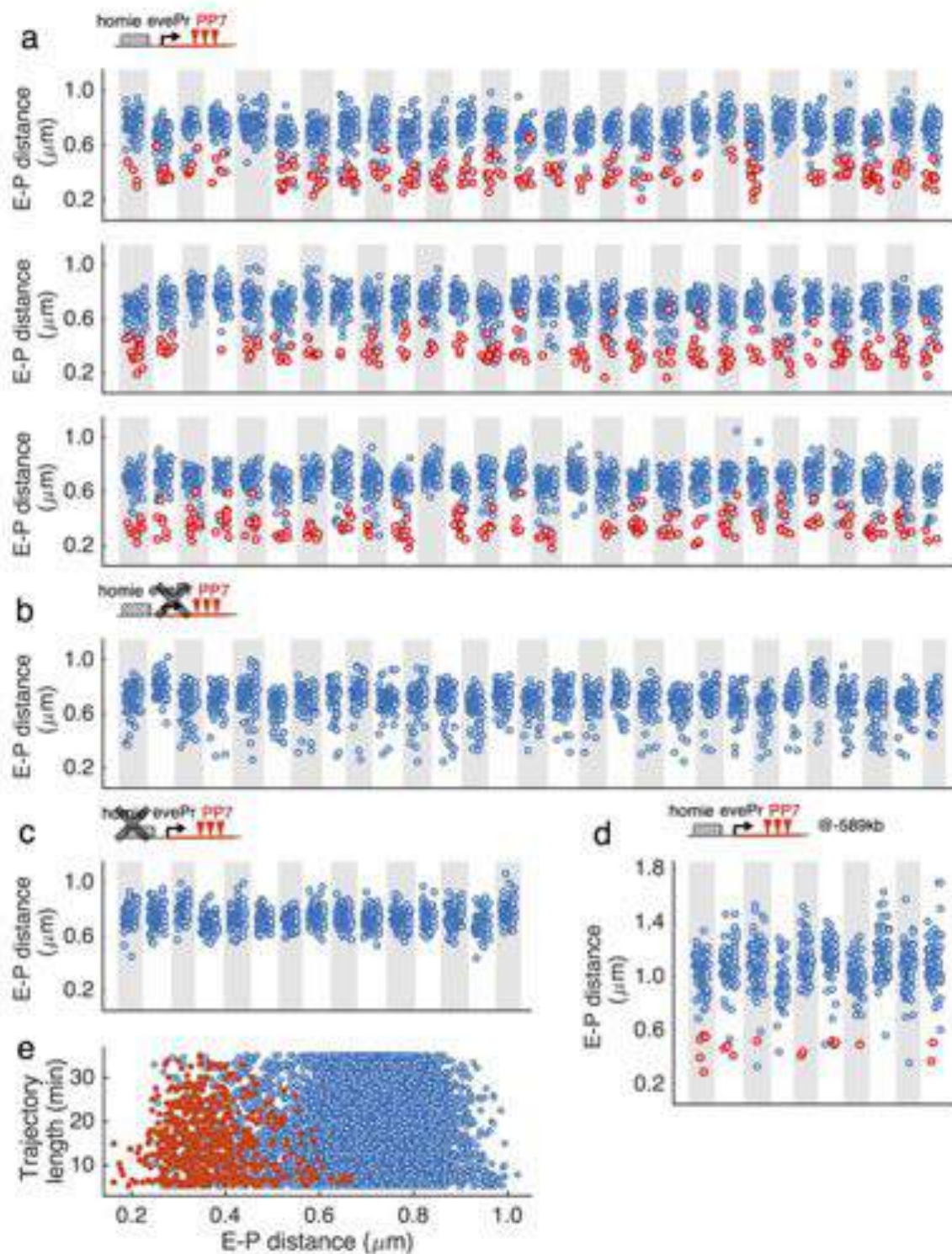
Supplementary Figure 5

Sustained physical proximity is required for transcription initiation and maintenance: individual traces.

a, Transcriptional activity (red spot (PP7) intensity) and instantaneous enhancer–promoter distance (blue-green distance) as a function of time for 286 nuclei transitioning from the Red-OFF to the Red-ON state. Time series for individual nuclei are aligned such that PP7

activity starts at 0 min (red dashed lines). Individual traces are sorted according to the mean enhancer–promoter distance in the 5 min before PP7 activity is observed. **b**, Distribution of the instantaneous enhancer–promoter distance as a function of time for the Red-OFF to Red-ON transition. Calculated from **a**. **c**, Transcription and instantaneous enhancer–promoter distance as a function of time for 203 nuclei transitioning from the Red-ON to the Red-OFF state. Time series for individual nuclei are aligned such that PP7 activity ends at 0 min (red dashed lines). Individual traces are sorted according to the mean enhancer–promoter distance in the 5 min before PP7 activity disappears. **d**, Distribution of the instantaneous enhancer–promoter distance as a function of time for the Red-ON to Red-OFF transition. Calculated from **c**.
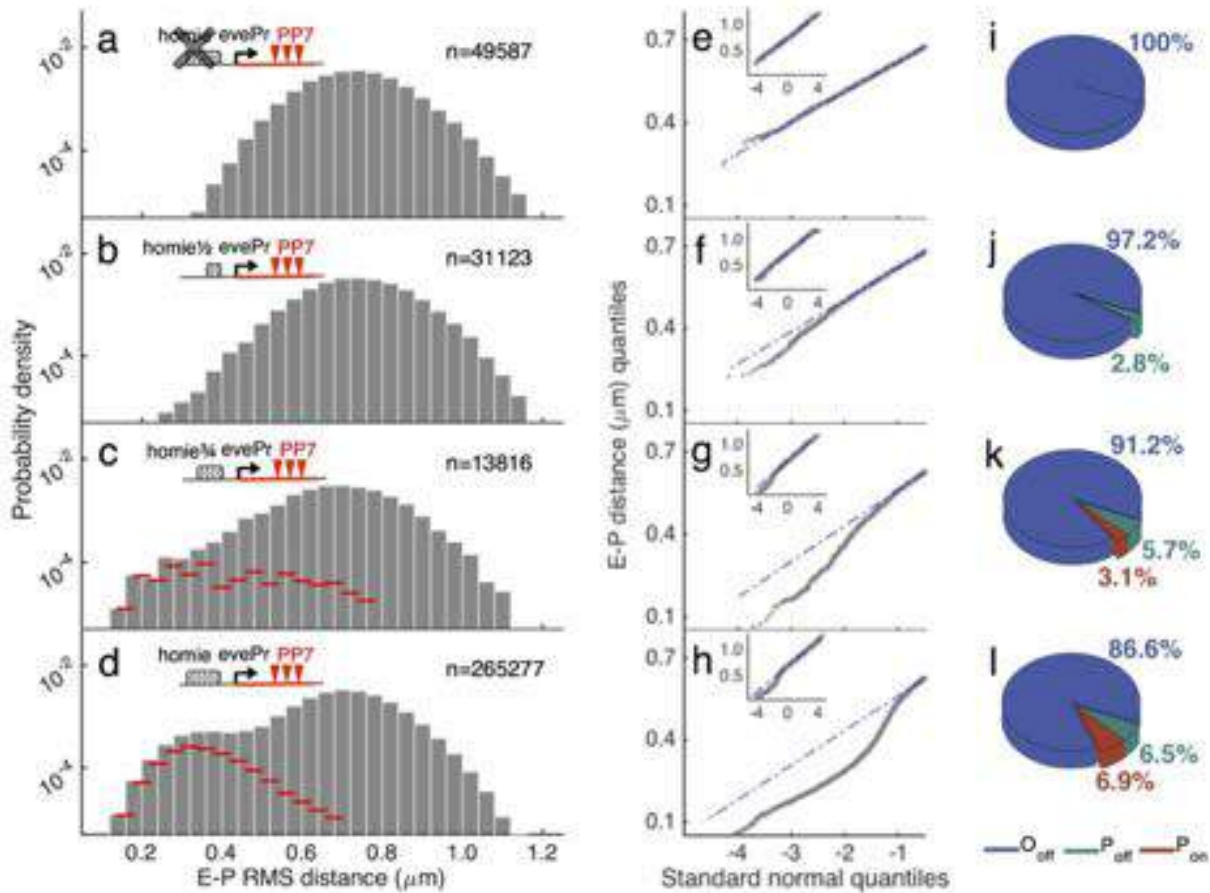
Supplementary Figure 6

Analysis of enhancer–promoter distance for individual embryos and individual nuclei.

a–c, The time-averaged RMS distance between MS2 (blue) and parS (green) spots (enhancer–promoter distance) is depicted as a scatterplot for each nucleus from 84 embryos carrying the *parS-homie-evePr-PP7* construct (**a**), 29 embryos carrying the *parS-homie-*

noPr-PP7 construct (**b**), and 15 embryos carrying the *parS-lambda-evePr-PP7* construct (**c**) located at −142 kb with respect to the *eve-MS2* locus. **d**, Time-averaged RMS enhancer–promoter distance for ten embryos carrying the *parS-homie-evePr-PP7* construct at −589 kb with respect to the *eve-MS2* locus. Data points marked in red are calculated from the Red-ON part of enhancer–promoter trajectories in nuclei displaying PP7 activity. Data points marked with blue are calculated from full enhancer–promoter trajectories in nuclei that never show PP7 during the imaging time window (25–55 min in nc14). Notice that the number of time points (e.g., length of enhancer–promoter trajectories) used for calculating RMS distance varies among nuclei depending on the nuclear anterior–posterior position and the view of the image. **e**, RMS enhancer–promoter distance as a function of the length of the trajectories used for RMS distance calculation. All RMS enhancer–promoter distance samples from the 84 embryos carrying the *parS-homie-evePr-PP7* construct at −142 kb are shown.
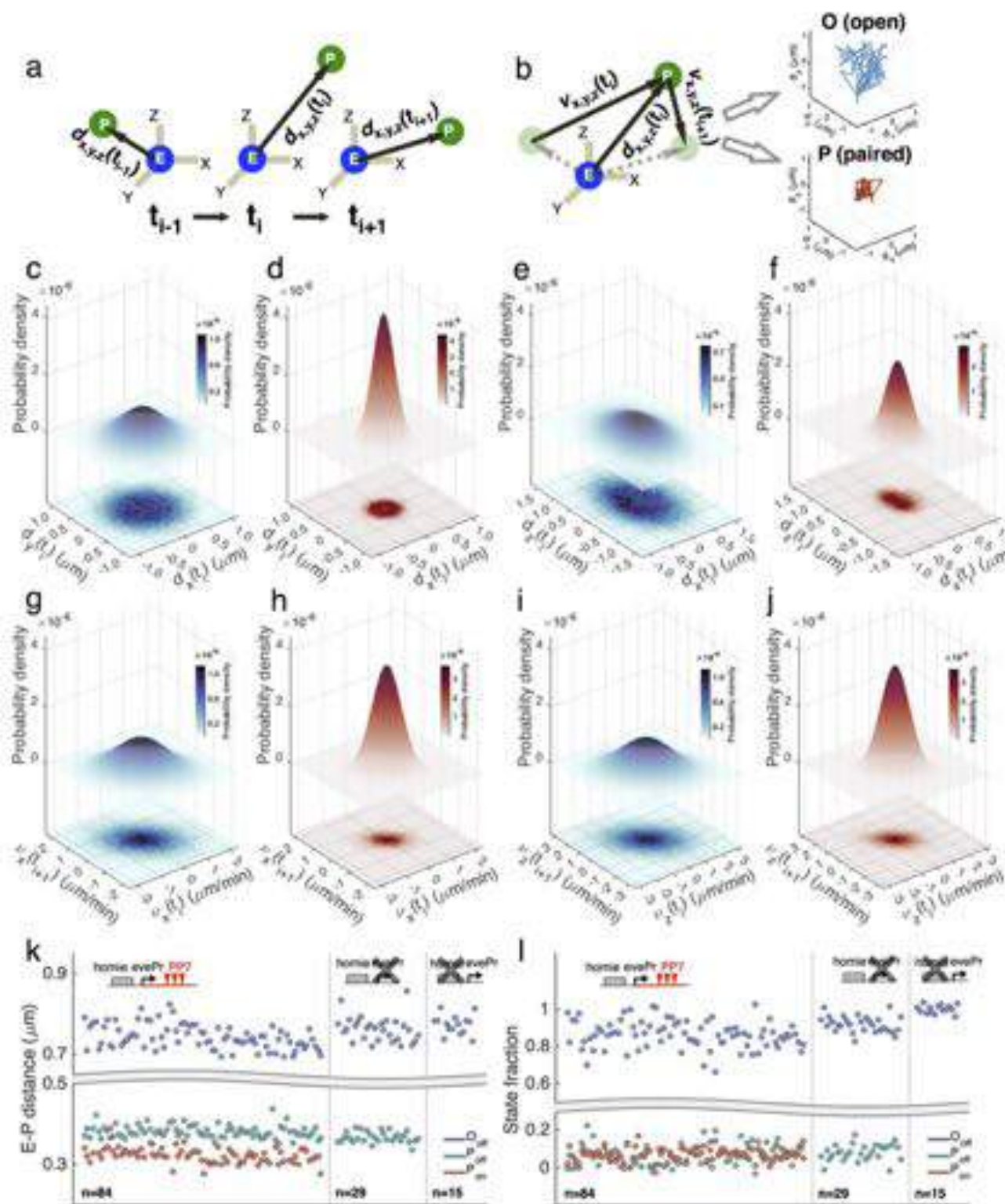
Supplementary Figure 7

Tuning stability of the *homie* element.

a–d, The enhancer–promoter distance (RMS distance) distribution for four experimental constructs: *parS-lambda-evePr-PP7* (**a**), *parS-homie½-evePr-PP7* (**b**), *parS-homie¾-evePr-PP7* (**c**) and *parS-homie-evePr-PP7* (**d**). A 5-min sliding window along each time trace is used to calculate RMS enhancer–promoter distances. *homie½* (chr2R:9,988,934–9,988,750, dm6) and *homie¾* (chr2R:9,989,025–9,988,750, dm6) are two truncated *homie* elements. Red bars in **c** and **d** show the probability density of RMS distance samples accompanied by continuous PP7 transcription. **e–h**, Quantile–quantile plots against the standard normal distribution for the RMS enhancer–promoter distances shown in **a–d**, respectively. Short enhancer–promoter distances resulting from the paired (P_{off} and P_{on}) states are progressively enriched as the stability of the *homie* element increases. Insets show the complete quantile–quantile plots. **i–l**, Fraction of each topological state for the constructs shown in **a–d**, respectively. See Supplementary Fig. 8 and the Methods for details about topological state classification.
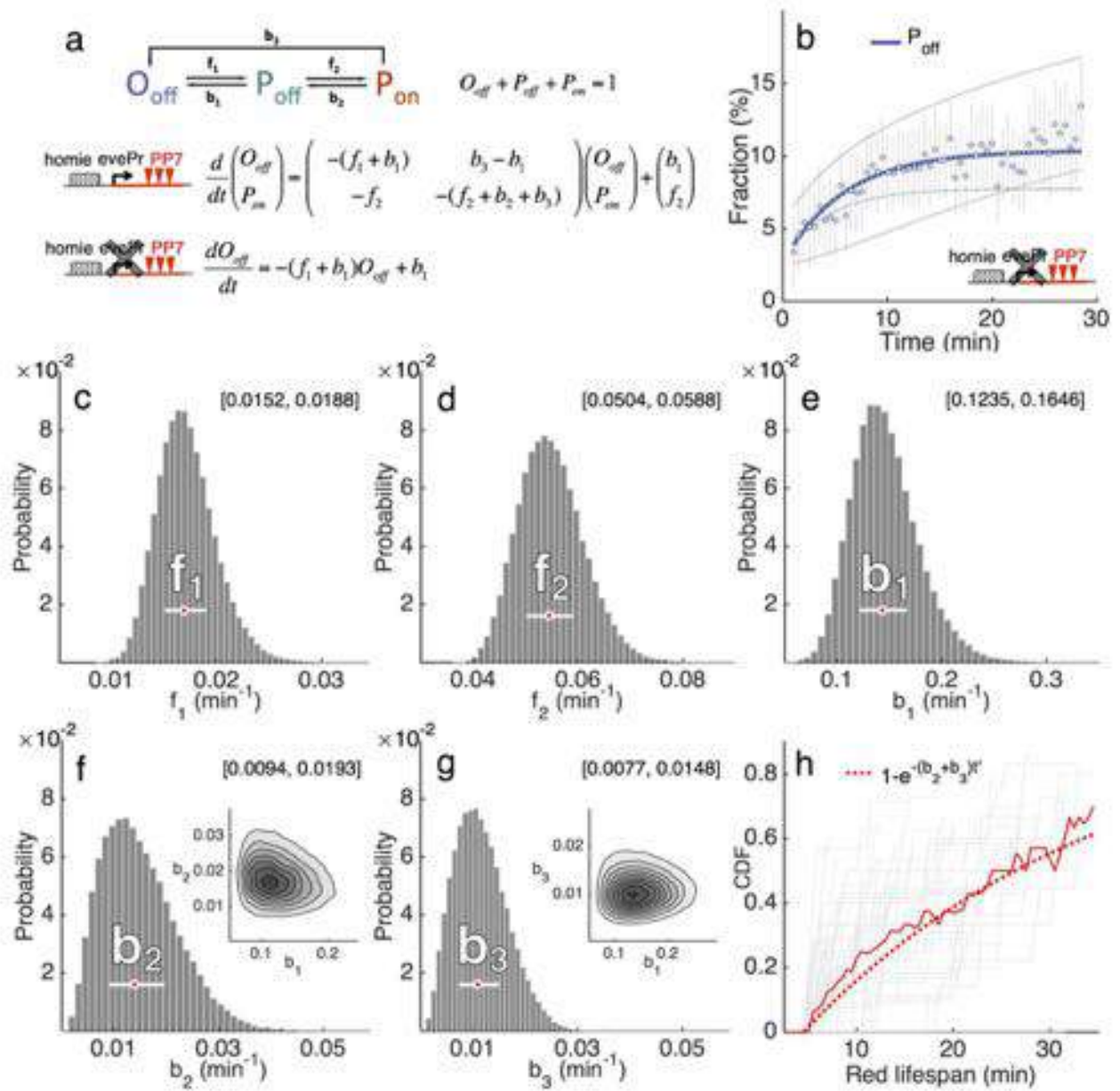
Supplementary Figure 8

Training of a Bayesian classifier and characterization of the three topological states.

a, An enhancer–promoter distance vector ($d_{x,y,z}$) is calculated at each time point, corrected for chromatic aberration. **b**, The relative

velocity ($v_{x,y,z}$) between the enhancer (blue MS2 spot) and promoter (green parS spot) is calculated from the two consecutive distance vectors. The instantaneous distance vector and the two velocity vectors that connect the two adjacent time points are used for training a binary classifier using a naive Bayes method (Methods). Two training samples are used. For the open state (O state), enhancer–promoter trajectories from the *parS-lambda-evePr-PP7* control are used. For the paired state (P state), enhancer–promoter trajectories from the Red-ON part of nuclei displaying PP7 activity are used. The last 4 min of these Red-ON trajectories are removed from the training sample because of PolII elongation. **c**–**f**, Joint distribution of the selected dimensions of the distance vectors for the O state (**c**,**e**) and P state (**d**,**f**) training samples. **g**–**j**, Joint distribution of the selected dimensions of the velocity vectors for the O state (**g**,**i**) and P state (**h**,**j**) training samples. From **c**–**j**, *z* projections are raw data and the probability density functions of 2D Gaussian fits are shown. **k**,**l**, RMS distance (**k**) and fraction (**l**) for each topological state calculated for individual embryos (*n* is the number of embryos).
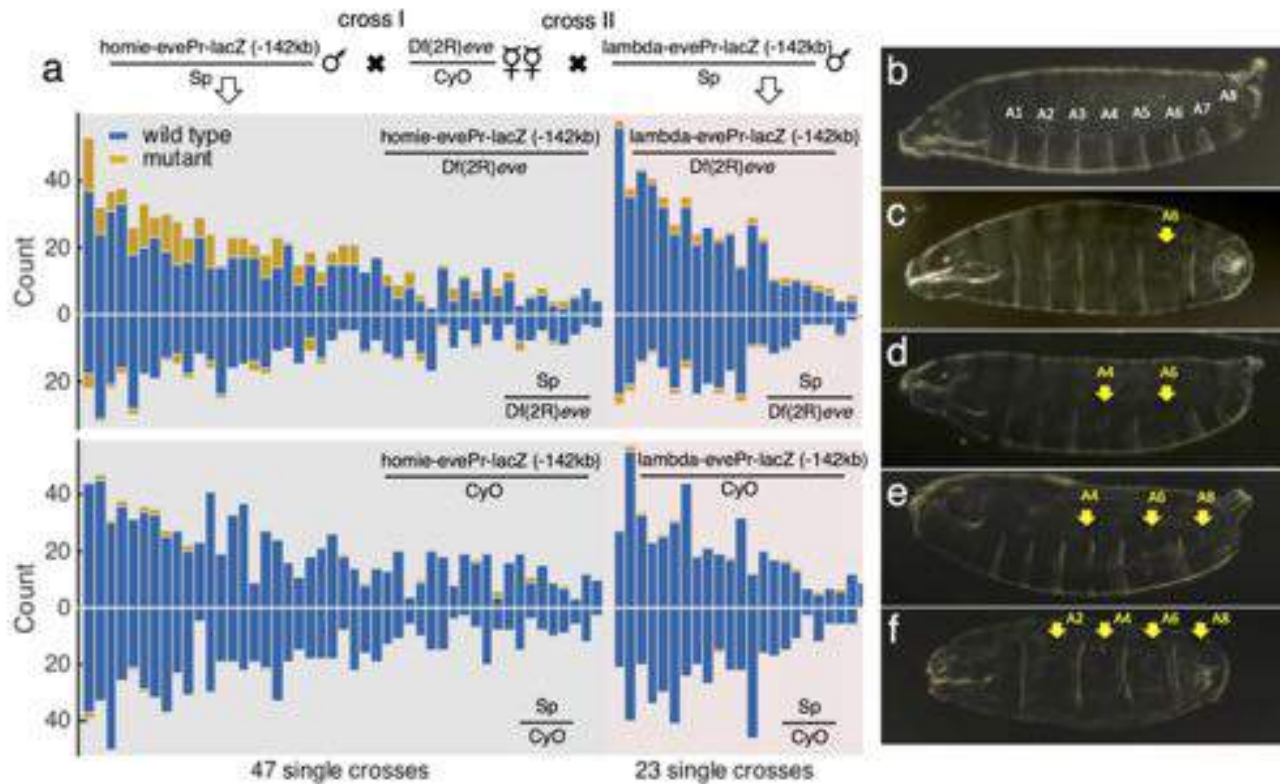
Supplementary Figure 9

A kinetic model captures transition rates among the three topological states.

a, A series of first-order reactions are used to model the transition kinetics between the O_{off}, P_{off} and P_{on} states. Based on the finding that physical proximity is required for transcriptional activation, we assume in this model that P_{on} occurs only after P_{off} is established. The coupled ODEs describe evolution of the system given the initial conditions. For *parS-homie-noPr-PP7*, only the O_{off} and P_{off} states are present and we assume the same f_1 and b_1 values as for *parS-homie-evePr-PP7*. **b**, Fraction of the P_{off} state for *homie-noPromoter-PP7* as a function of developmental time. 0 on the *x* axis corresponds to 25 min in nc14. The mean ± SE is shown (*n* = 29 embryos). This curve, together with time series curves obtained from the *parS-homie-evePr-PP7* construct (dashed lines; same as in Fig. 3e), is used to infer the kinetic parameters with Markov chain Monte Carlo (MCMC) simulations (Methods). **c–g,** Marginal posterior distributions of the five kinetic parameters in **a** constructed from 90,000 stationary MCMC samples. Medians are labeled. Error bars span from the 25th-percentile to the 75th-percentile quantile (also shown in square brackets). Insets in **f** and **g** show the joint distribution of (b_1, b_2) and (b_1, b_3), respectively. Darker color represents higher density. **h**, The inferred parameters for the disappearance of P_{on} recapitulate the distribution of lifespans of PP7 activity. To calculate PP7 lifespan distribution, PP7 traces are

grouped into cohorts according to the maximum measurable lifespan for each trace (Methods). For each PP7 cohort, a cumulative distribution function (CDF) for the PP7 lifespan is calculated (gray curves). Because the lifespan distribution is truncated at the maximum measurable time, the tails of the CDFs (corresponding to CDF = 1) are removed. The solid red line shows the median of these truncated CDFs, which is the CDF of the lifespans of PP7 activity. The dashed red curve comes from the CDF of an exponential distribution with mean = $(b_2 + b_3)^{-1}$ = $(0.014 + 0.011)^{-1}$ min. This exponential CDF is shifted horizontally to account for a deterministic elongation time of 4 min, which coincides with the lifespan of the shortest PP7 trace.

Supplementary Figure 10

Scoring mutant phenotypes resulting from promoter competition.

a, Cross schemes to test the phenotypic effects of competition between the endogenous *eve* promoter and the ectopic *eve* promoter that is activated upon the formation of new topological states. Single males, either *homie-evePr-lacZ* or *lambda-evePr-lacZ*, are used for the crosses (note removal of PP7 sequences). For each single cross, the patterning phenotypes in adult abdominal segments A4, A6 and/or A8 are scored. No conspicuous phenotype in other abdominal segments is noticed. **b**–**f**, The adult abdominal phenotypes most likely result from haploinsufficiency of *eve*, as shown in the cuticles derived from a cross between homozygous *homie-evePr-lacZ* males and *Df*(2R)*eve-/CyO* females. A wild-type cuticle is shown in **b**. Strong *eve* phenotypes, i.e., loss or perturbation of denticle bands in the even-numbered abdominal segments, are observed (**c**–**f**).